Acta Geochim (2025) 44:805–825
https://doi.org/10.1007/s11631-025-00792-9

ORIGINAL ARTICLE

Petrogenesis of the dioritic rocks in the eastern North Qaidam: Implications for the tectonic evolution of the Paleo-Tethys Ocean

Panlong Wang[1,2] · Yongjun Li[2,3] · Yujun Zhuang[1] · Pingyang Gu[1] · Chao Shi[1] · Jiaxin Yan[1] · Gaoxue Yang[2,3] · Wei Li[2] · Hai Li[4] · Jianye Zhang[2] · Hao Fu[2]

Received: 30 December 2024 / Revised: 1 May 2025 / Accepted: 20 May 2025 / Published online: 18 June 2025

Abstract Numerous Indosinian igneous rocks in the North Qaidam (NQ) provide crucial insights into the tectonic evolution of the Paleo-Tethys Ocean. This paper presents a comprehensive study of the petrography, mineralogy, geochemistry, zircon U–Pb geochronology, and Hf isotope composition of dioritic rocks from the eastern NQ. Zircon U–Pb dating results indicate that the dioritic rocks were formed during the Middle Triassic (244–240 Ma). The rocks exhibit high-K calc-alkaline characteristics with variable SiO_2 (55.25–65.39 wt%) and elevated $K_2O + Na_2O$ (4.81–6.94 wt%) contents. They show enrichment in LILEs (Rb, Ba, K) and depletion in HFSEs (Nb, Ta, Ti), with slight negative Eu anomalies (Eu/Eu* = 0.89–0.97). Zircon $\varepsilon_{Hf}(t)$ values (−20.93 to + 5.60) and T_{DM2} ages (0.85–1.72 Ga) suggest mixed sources. Petrographic and mineralogical analysis reveals that the plagioclase phenocrysts exhibit disequilibrium textures (including reverse zoning), primarily composed of andesine and labradorite, with a small amount of oligoclase. The clinopyroxenes are all augites and have high crystallization temperatures (1111–1151 °C). These features, particularly the reverse zoning of plagioclase, support a petrogenetic model involving mantle-derived magma underplating that induced melting of ancient lower crust, followed by mixing of underplated basaltic magma with crust-derived felsic magma. Our results indicate formation in a back-arc extensional setting during subduction of the Zongwulong Paleo-Tethys Ocean.

Keywords Diorite · Magma mixing · Paleo-Tethys Ocean · Indosinian · North Qaidam

1 Introduction

The global Tethyan tectonic domain spanning Eurasia is primarily controlled by the opening and closing history of the Proto-, Paleo-, Meso-, and Neo-Tethys Ocean, experiencing a complex process involving multiple ocean basins, subductions, collisions, and orogenic events (Fig. 1a; Zhao et al. 2018a; Wu et al. 2020). The tectonic evolution of the Asian Tethys Ocean indicates that its orogenic processes have generated abundant natural resources (Metcalfe 2021; Li 2024). The Qinling-Qilian-Kunlun Central Orogenic Belt is a significant component of the Asian Tethys tectonic domain, preserving rich and significant amalgamation records of numerous terranes. Consequently, the Central Orogenic Belt serves as an exceptional window for investigating the tectonic evolution and mineralization of the Tethyan domain (Dong et al. 2018, 2021; Zhao et al. 2018a; Allen et al. 2023; Fu et al. 2024).

The NQ, located in the northern part of the Tibetan Plateau, is an important component of the Central Orogenic Belt that traverses mainland China (Fig. 1a). It serves as a natural

Supplementary Information The online version contains supplementary material available at https://doi.org/10.1007/s11631-025-00792-9.

✉ Yongjun Li
yongjunl@chd.edu.cn

✉ Gaoxue Yang
mllygx@126.com

[1] Xi'an Centre of Geological Survey, China Geological Survey, Xi'an 710054, China

[2] School of Earth Science and Resources, Chang'an University, Xi'an 710054, China

[3] Key Laboratory of Western China's Mineral Resources and Geological Engineering, Ministry of Education, Xi'an 710054, China

[4] School of Earth Sciences and Engineering, Xi'an Shiyou University, Xi'an 710065, China

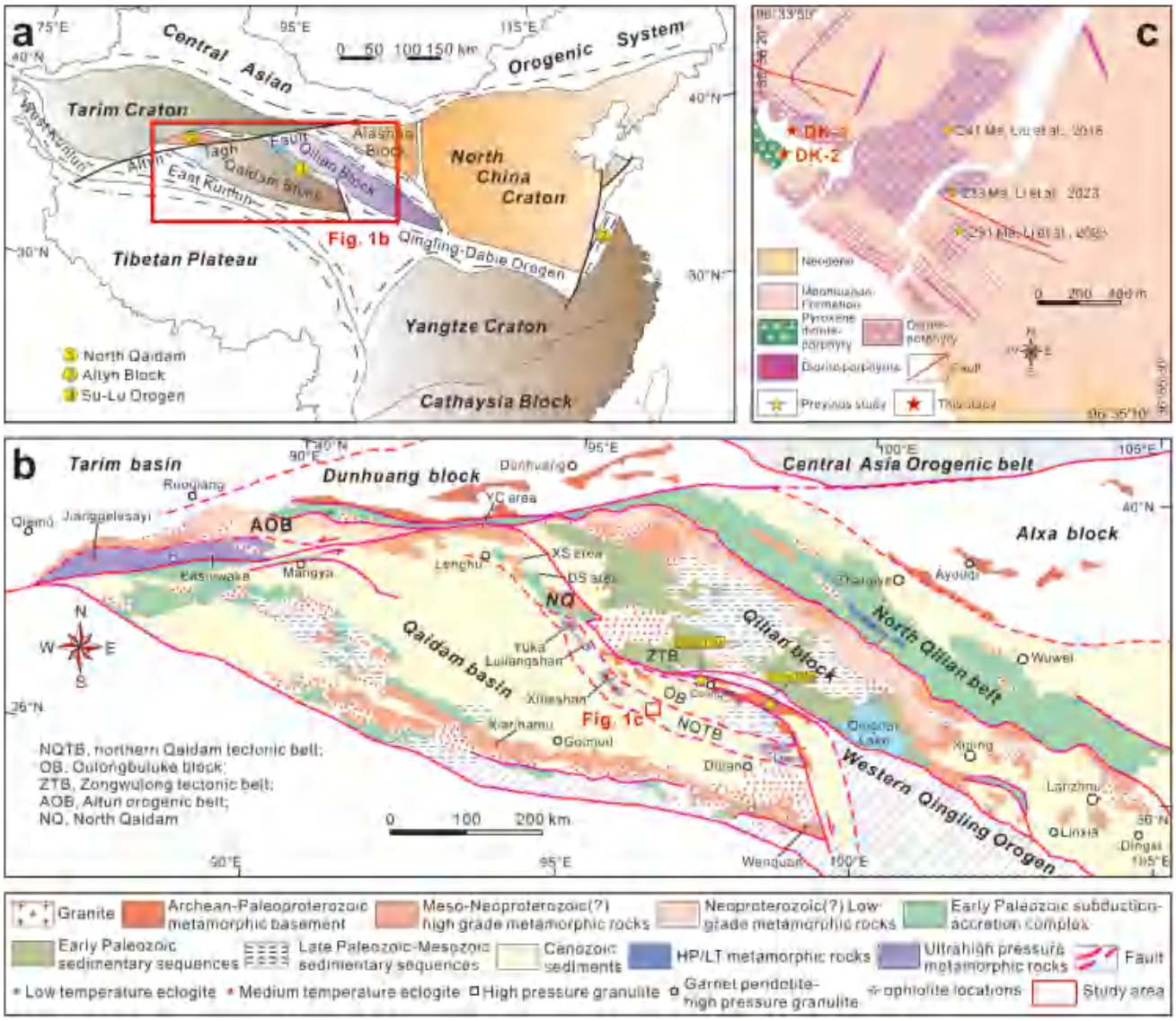

Fig. 1 Tectonic framework of the NQ and surrounding regions **a**, modified after Xia et al. 2016), geological map of the NQ (**b**, modified after Zhang et al. 2017), and detailed geological map in the Dadakenwulashan area of the NQ with the sampling locations (**c**, modified after Li et al. 2023). The literature data of ophiolites are from Wang et al. 2001 and Xu et al. 2019

laboratory for studying the Tethyan tectonic evolution and mineralization of the Tibetan Plateau. This orogenic belt is characterized by the development of large-scale Early Paleozoic (Shi et al. 2006; Wang et al. 2014; Zhao et al. 2018b; Sun et al. 2020a; Cai et al. 2021; Niu et al. 2021; Zhou et al. 2021; Li et al. 2022a) and Late Paleozoic-Early Mesozoic (Gehrels et al. 2003; Guo et al. 2009; Wu et al. 2009; Chen et al. 2012a; Cheng et al. 2017; Li et al. 2023; Wang et al. 2023, 2024a) igneous rocks, which record the composite tectonic evolution process from the Proto-Tethys to the Paleo-Tethys (Wu et al. 2019, 2025; Li et al. 2023; Wang et al. 2023, 2024a). Compared to the Early Paleozoic, Late Paleozoic-Early Mesozoic intrusive rocks are relatively less exposed (Wang et al. 2023, 2024a). Previous studies have revealed that the western NQ is characterized by Permian I-type granitic intrusives, with a small number of Carboniferous-Permian gabbros and Triassic granites (Wang et al. 2024a, 2025). In contrast, the eastern NQ is characterized by a large number of Late Permian-Triassic granitic intrusives, including some intermediate-mafic rocks. Among them, the granites are mainly magma-mixed I-type granites (Niu et al. 2018; Li et al. 2022b) and a small amount of Late Triassic A-type granites (Guo et al. 2009; Chen 2011). However, compared to previous studies on granites and mafic rocks, there has been little research on intermediate rocks, especially regarding their magma source composition and genesis mechanisms, which remain poorly constrained. Furthermore, the tectonic evolution process of the Late Paleozoic-Early Mesozoic (P–T) Paleo-Tethys Ocean in the NQ remains

highly debated, with six main competing hypotheses proposed in previous studies: (1) formation in an extensional setting from late collisional orogeny to post-orogenic stage (Wang et al. 2022); (2) intracontinental subduction after Paleo-Tethys Ocean closure (Wu et al. 2009); (3) oblique collision between West Qinling and Qaidam blocks (Peng et al. 2016); (4) northward subduction of the Buqingshan-A'nimaqing Ocean (Niu et al. 2018; Sun et al. 2022; Li et al. 2023; Shi et al. 2024; Wang et al. 2024b); (5) subduction of the Zongwulong Paleo-Tethys Ocean (Wang et al. 2001, 2023, 2024a, 2025; Guo et al. 2009); (6) combined effects of both oceanic systems (Wu et al. 2019). Among these, the most vigorous debate centers on two end-member models: (1) the northward subduction hypothesis (Model 4) versus (2) the southward subduction hypothesis (Model 5). This dichotomy essentially reflects the fundamental question of whether there was a complete tectonic-magmatic cycle of Paleo-Tethys Ocean subduction and closure in the NQ during this period (Wang et al. 2024a). Resolving this controversy is critical for understanding the Paleo-Tethys evolution.

Lead–zinc ore bodies, accompanied by silver mineralization, have been discovered in the Dadakenwulashan area located in the eastern NQ, which holds significant economic importance (Liu et al. 2018a, b). The ore bodies are mainly hosted within dioritic rocks and the Maoniushan Formation. Previous studies have been conducted on the Maoniushan Formation and the geological characteristics of the deposit (Liu et al. 2018b), but research on the dioritic rocks, which is closely related to mineralization within the mining area, is extremely limited, and there are controversies regarding its petrogenesis: (1) The diorite was formed at 241 Ma through partial melting of the lithospheric mantle contaminated by continental crust (Liu et al. 2018a); (2) Tthe Diorite and diorite-porphyrite dikes were formed at 233–231 Ma through partial melting of the ancient mafic lower crust, accompanied by the addition of a small amount of mantle-derived material (Li et al. 2023). Therefore, this study selected the unstudied dioritic rocks in the western part of the Dadakenwulashan pluton for petrographic, mineralogical, geochemical, zircon U–Pb geochronological, and in situ Lu–Hf isotopic studies. Combining previous research results, the petrogenesis and tectonic setting of the Dadakenwulashan pluton were discussed, aiming to provide insights into the tectonic-magmatic evolution of the Paleo-Tethys in the NQ and to support further ore prospecting efforts in the area.

2 Geological background and sample descriptions

The NQ extends in a northwest-southeast direction from Altun Mountain to Ela Mountain. It is bounded to the east by the Wahongshan Fault, to the west by the left-lateral strike-slip Altun Tagh Fault, to the south by the North Qaidam Fault, connecting with the Qaidam Basin, and to the north by the southern margin of the Middle Qilian Fault, adjoining the Qilian Block. It is a multi-unit composite tectonic belt with diverse compositions, frequent magmatic activities, and complex metamorphic and deformational processes (Guo et al. 2009; Song et al. 2014; Peng et al. 2019; Yu et al. 2021). Bounded by the Zongwulong-Qinghainanshan Fault and Yuka Fault, the NQ can be divided into three structural units from north to south: the Zongwulong Tectonic Belt, the Oulongbuluke Block, and the Northern Qaidam Tectonic Belt (Fig. 1b).

The Zongwulong Tectonic Belt is positioned between the Qilian and the Oulongbuluke blocks, extending northwest towards the Altun Tagh Fault and southeast to the Qinghainanshan region. It is composed of the Late Paleozoic Zongwulong Group, the Early-Middle Triassic Junzihe Group, and ophiolites (Wang et al. 2001; Guo et al. 2009; Fu et al. 2021; Li et al. 2024). Ophiolites are predominantly found in the Tianjunnanshan and Zongwulongshan areas, with zircon U–Pb ages of 509 ± 4 Ma (Fu et al. 2021) and 318 ± 3 Ma (Wang et al. 2001) from Tianjunnanshan ophiolite and 300.7 ± 1.4 Ma from volcanic rocks in Zongwulongshan ophiolite (Xu et al. 2019). These indicate that the Zongwulong Tectonic Belt may be an Early Paleozoic-Early Mesozoic composite tectonic belt formed by the successive closure of the Proto-Tethys and Paleo-Tethys oceans (Fu et al. 2021). The Oulongbuluke Block comprises Paleoproterozoic metamorphic crystalline basement (Delingha Complex, Dakendaban Group, and Wandonggou Group) and sedimentary cover, unconformably overlying it since the Neoproterozoic (Lu et al. 2008; Chen et al. 2009; Fu et al. 2022; Sun et al. 2019, 2020b). It is considered a continental fragment with craton properties (Chen et al. 2009, 2012b; Sun et al. 2019). The Northern Qaidam Tectonic Belt is mainly composed of ultrahigh-pressure metamorphic rocks, the Tanjianshan Group, and ophiolites (Song et al. 2014; Li et al. 2023; Fu et al. 2024), representing products of different stages of evolution of the Proto-Tethys Ocean during the Early Paleozoic to early Late Paleozoic.

The study area is located in the Dadakenwulashan area of the eastern NQ. The fault structures within the area are relatively developed, but their overall scale is relatively small, with two main sets of faults trending northwest-southeast and nearly east-west. The exposed stratigraphic units within the area primarily include the Middle-Late Devonian Maoniushan Formation and the Pliocene Youshashan Formation. The Maoniushan Formation is composed of agglomerate, volcanic breccia, volcanic lava, tuff, tuffaceous rocks containing volcaniclastic sediments, and slate, claystone, siltstone, and sandy conglomerate (Li et al. 2023). The Youshashan Formation consists of polymictic conglomerate, fine sandstone, mudstone, and siltstone bands. The Dadakenwulashan pluton occurs as a

stock in the southern part of the study area (Fig. 1c), showing a bay-shaped intrusive contact relationship with the Maoniushan Formation. It is approximately 1.8 km long in the northeast-southwest direction and 1.4 km long in the northwest-southeast direction, with an exposed area of approximately 0.8 km^2. Additionally, the dioritic dikes exposed in the southern part of the pluton mainly intrude densely into the Maoniushan Formation, with scattered distributions also observed in the northwest. They exhibit a regular linear distribution with strikes roughly ranging from 130° to 140°, lengths of tens of meters to 1 km, and dike widths of 0.5 to 7.0 m. Previous studies have indicated that the lithology of this pluton and the dioritic dikes is mainly composed of diorite and diorite-porphyrite (Liu et al. 2018a; Li et al. 2023), and zircon U–Pb ages of 241 Ma (Liu et al. 2018a) and 233–231 Ma (Li et al. 2023) were obtained from diorite and diorite-porphyrite dikes in the eastern part of the pluton, respectively.

To ensure the freshness and representativeness of the rock samples, this study collected samples from locations far away from stratigraphic contact zones, alteration zones, and fault zones. Two samples were collected from the unstudied dioritic rocks (diorite-porphyrite and pyroxene diorite-porphyrite) in the western part of the Dadakenwulashan pluton for zircon U–Pb geochronology and in situ zircon Lu–Hf isotope studies, 2 samples for mineralogical electron microprobe analysis, and 12 samples for petrogeochemical studies. The sampling locations, field characteristics, and petrographic characteristics of the samples are shown in Figs. 1c and 2.

The dioritic rocks intrude into the volcanic rocks of the Maoniushan Formation and are later intruded by diorite-porphyrite dikes (Fig. 2a, b).

The diorite-porphyrite exhibits a porphyritic texture and massive structure (Fig. 2c). The phenocrysts are plagioclase (~35%) and hornblende (~5%). The plagioclase appears as euhedral to subhedral plates, exhibiting polysynthetic

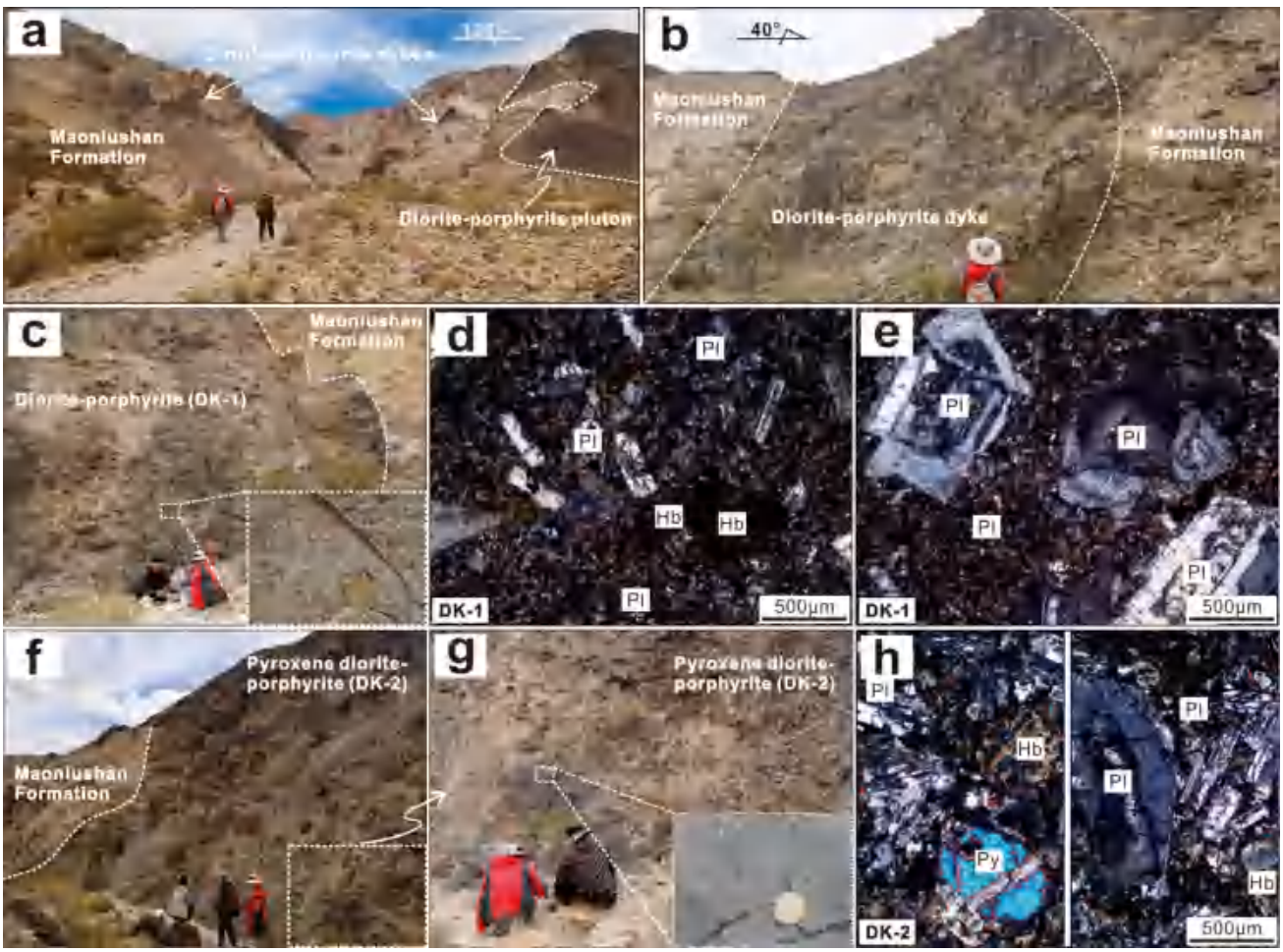

Fig. 2 Representative field photographs, hand specimen photographs, and microscopic photographs for dioritic rocks in the Dadakenwulashan area of the NQ. **a** and **b** Dioritic rocks intrude into the volcanic rocks of the Maoniushan Formation; **c**, **d**, and **e** diorite-porphyrite (DK-1); **f**, **g**, and **h** pyroxene diorite-porphyrite (DK-2). Pl, plagioclase; Hb, hornblende; Py, pyroxene

twinning and zoning structures, and is mostly altered to clay and sericite. The hornblende is mostly pseudomorphed. The matrix is mainly composed of plagioclase (~ 20%), hornblende (~ 20%), cryptocrystalline material (~ 18%), and biotite (~ 1%). The accessory minerals are primarily apatite (Fig. 2d, e).

The pyroxene diorite-porphyrite also exhibits a porphyritic texture and massive structure (Fig. 2f, g). The phenocrysts are primarily plagioclase (~ 30%), followed by hornblende (~ 4%) and clinopyroxene (~ 2%). The plagioclase appears as euhedral to subhedral plates, exhibiting polysynthetic twinning and zoning structures, and is mostly altered to clay and sericite. The hornblende occurs as euhedral to subhedral columns, mostly pseudomorphed by chlorite. The clinopyroxene appears as euhedral to subhedral columns. The matrix is mainly composed of plagioclase (~ 33%) and hornblende (~ 15%), followed by cryptocrystalline material (~ 15%). The accessory minerals include apatite, which is scattered throughout the matrix (Fig. 2h).

3 Analytical methods and results

The analytical methods in this study including zircon U–Pb dating, in situ zircon Hf isotopes, and whole-rock and mineral major and trace element geochemistry analyses, are described in the Supplementary Text S1. The corresponding analysis results are listed in Supplementary Tables S1–S5.

3.1 Mineral compositions

Mineral composition analysis was conducted on plagioclase in diorite-porphyrite and pyroxene and plagioclase in pyroxene diorite-porphyrite, with the structural formulas of plagioclase and pyroxene calculated based on eight and six oxygen atoms, respectively. The mineral analysis results for plagioclase and pyroxene are listed in Supplementary Tables S1 and S2.

The cores of plagioclase phenocrysts in diorite-porphyrite have undergone relatively intense dissolution, while the edges have not experienced significant dissolution and are mainly composed of oscillatory zoning. The plagioclase exhibits complex compositional zoning, with some phenocrysts displaying inverse zoning structures (Fig. 3a-f). The cores have lower An values, mostly belonging to andesine, with a very small number being oligoclase (Fig. 3p). The edges have higher An values and relatively consistent compositions, belonging to andesine and labradorite (Fig. 3p). A few plagioclase phenocrysts exhibit normal zoning structures (Fig. 3g-i), with higher An values in the cores (labradorite and andesine) and lower An values in the edges, mostly andesine (Fig. 3p). The plagioclase phenocrysts in pyroxene diorite-porphyrite do not show obvious zoning structures and have relatively consistent compositions (Fig. 3n-r), mostly belonging to labradorite, with a small amount being andesine (Fig. 3p).

Clinopyroxene phenocrysts occur only in the pyroxene diorite-porphyrite samples and are mainly augite (Fig. 3j–m, q). The phenocrysts have relatively high MgO (13.6–15.5 wt%), FeO (9.82–12.9 wt%), and CaO (17.5–19.2 wt%) contents, with $Mg^{\#}$ values of 67.5–74.2. The grains are characterized by relatively low contents of TiO_2 (0.47–0.99 wt%), Al_2O_3 (2.03–3.45 wt%), and Na_2O (0.25–0.59 wt%). The clinopyroxene thermobarometer yielded temperatures of 1111–1151 °C (Wang et al. 2021) and pressures of 0.80–4.09 kbar (Wang et al. 2021).

3.2 Zircon U–Pb geochronology

Two representative samples were selected for zircon U–Pb analysis, including diorite-porphyrite (DK-1) and pyroxene diorite-porphyrite (DK-2). The results are given in Table S3 and illustrated in Fig. 4.

Zircons from diorite-porphyrite and pyroxene diorite-porphyrite are transparent to subtransparent prismatic grains (Fig. 4a-d). Most of these grains show an internal structure with oscillatory zoning, and several of them have inherited cores in CL (Fig. 4a, c). The grains are generally 40–100 μm wide and 50–200 μm long with length-width ratios in the range of 1:1 to 2:1. Moreover, all zircon grains have variable abundances of Th (1–6226 ppm) and U (33–6780 ppm) with resulting high Th/U ratios of 0.11–2.78 (five zircon grains exhibit lower Th/U ratios of 0.004–0.09, indicating a possible metamorphic origin), suggesting that most of these zircon grains are magmatic in origin.

The six analytical points in the diorite-porphyrite do not fall on the concordia line; therefore, they are not included in the subsequent analysis. Among the remaining 34 analytical points, 8 yielded relatively consistent $^{206}Pb/^{238}U$ ages (236–246 Ma) with Th/U ratios ranging from 0.38 to 1.15. On the U–Pb age concordia diagram, these points are densely distributed along the concordia line (Fig. 4b). Their weighted mean age is 240.1 ± 3.4 Ma (MSWD = 0.39, $n = 8$), which represents the emplacement age of the diorite-porphyrite. The remaining 26 analytical points yielded older $^{206}Pb/^{238}U$ ages (310–2369 Ma), which are far from the age concentration area and belong to captured old zircons.

One analytical point in the pyroxene diorite-porphyrite does not fall on the concordia line and is therefore excluded from further analysis. Among the remaining 39 analytical points, eight analytical points yielded relatively consistent $^{206}Pb/^{238}U$ ages (240–249 Ma) with Th/U ratios ranging from 0.50 to 0.79. On the U–Pb age concordia diagram, these points are densely distributed along the concordia line (Fig. 4d). Their weighted mean age is 243.9 ± 3.4 Ma (MSWD = 0.43, $n = 8$), which

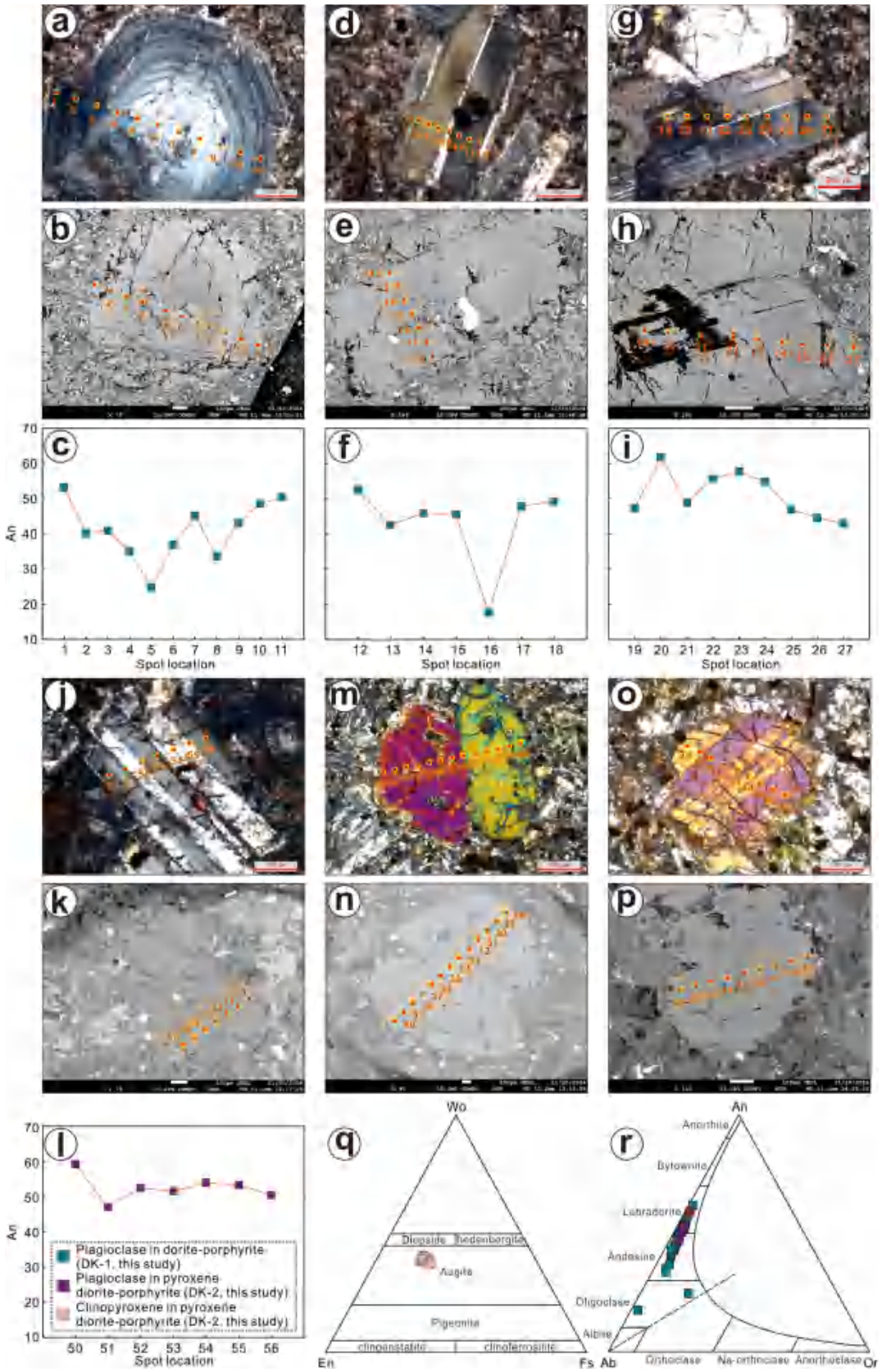
a
d
g
b
e
h
c
f
i
An
Spot location
j
m
o
k
n
p
l
q
r
Plagioclase in dorite-porphyrite (DK-1, this study)
Plagioclase in pyroxene diorite-porphyrite (DK-2, this study)
Clinopyroxene in pyroxene diorite-porphyrite (DK-2, this study)
Wo
En
Fs
Diopside
Hedenbergite
Augite
Pigeonite
clinoenstatite
clinoferrosilite
An
Ab
Or
Anorthite
Bytownite
Labradorite
Andesine
Oligoclase
Albite
Orthoclase
Na-orthoclase
Anorthoclase

◂**Fig. 3** Cross-polarized photomicrograph, back-scattered electron (BSE) images, and geochemical profiles for dioritic rocks in the Dadakenwulashan area of the NQ. **a**–**i** Plagioclases in diorite-porphyrite (DK-1) showing dissolution textures and oscillatory zoning in An content; **j**–**l** plagioclase in pyroxene diorite-porphyrite showing multiple twin and relatively stable An content with larger An contents on individual edges; **m**–**p** clinopyroxenes in pyroxene diorite-porphyrite showing multiple twins; **q** classification diagram of clinopyroxene (Morimoto 1988); **r** classification diagram of plagioclase

represents the emplacement age of the pyroxene diorite-porphyrite. The remaining 30 analytical points yielded older $^{206}Pb/^{238}U$ ages (262–2545 Ma), which are far from the age concentration area and belong to captured zircons. Additionally, one analytical point yielded a younger $^{206}Pb/^{238}U$ age (215 Ma), perhaps because of later metamorphic genesis.

3.3 Major and trace element geochemistry

Six diorite-porphyrite (DK-1-1 ~ DK-1-6) and six pyroxene diorite-porphyrite (DK-2-1 ~ DK-2-6) samples were collected for whole-rock major and trace element analysis (Table S4).

The six diorite-porphyrite samples have high SiO_2 (64.95–65.39 wt%), Al_2O_3 (16.40–16.75 wt%), and K_2O (3.00–3.18 wt%), low TiO_2 (0.63–0.65 wt%), Fe_2O_3T (4.70–5.11 wt%), MgO (1.88–2.06 wt%), and CaO (3.35–3.86 wt%) contents, $Mg^{\#}$ (43–45) values, Cr (14.4–21.3 ppm), and Ni (4.86–7.30 ppm) concentrations. All the samples are plotted in the granodiorite field in the $Na_2O + K_2O$ versus SiO_2 diagram (Fig. 5a) and show high-K calc-alkaline affinity in the K_2O versus SiO_2 diagram (Fig. 5b). The samples show light rare earth element (LREE) enrichment and subparallel right-sloping patterns with $(La/Yb)_N = 22.0–25.4$, $(Gd/Yb)_N = 2.31–2.54$, and $Eu/Eu^* = 0.87–0.91$ in the chondrite-normalized rare earth element (REE) diagram (Fig. 6a). They have arc-like primitive mantle (PM)-normalized patterns with enrichment in LILEs and depletion in HFSEs (e.g., Nb, Ta, and Ti; Fig. 6b).

Compared with the diorite-porphyrite samples, the six pyroxene diorite-porphyrite samples have lower SiO_2 (55.25–56.59 wt%) and K_2O (1.50–2.08 wt%) contents but have higher TiO_2 (1.10–1.19 wt%), Al_2O_3 (17.55–17.96 wt%), Fe_2O_3T (8.25–8.94 wt%), MgO (4.15–5.16 wt%), CaO (4.92–7.05 wt%) contents, $Mg^{\#}$ (50–53) values, Cr (21.7–42.9 ppm), and Ni (9.97–14.2 ppm) concentrations. The samples plot in the Gabbroic diorite field (Fig. 5a), and belong to a calc-alkaline to high-K calc-alkaline series (Fig. 5b). They also show LREE enrichment and subparallel right-sloping patterns [$(La/Yb)_N = 11.3–12.0$, $(Gd/Yb)_N = 2.22–2.552$, and $Eu/Eu^* = 0.87–0.97$] (Fig. 6a) and have arc-like characteristics (Fig. 6b).

3.4 Zircon in situ Hf isotopes

In situ Hf isotope analyses were performed on zircons from the diorite-porphyrite and pyroxene diorite-porphyrite at the same spots as the U–Pb dating. The results are listed in Supplementary Table S5 and illustrated in Fig. 7.

Eight spots from diorite-porphyrite with apparent ages have $^{176}Yb/^{177}Hf$ and $^{176}Lu/^{177}Hf$ ratios of 0.001197–0.041246 and 0.000035–0.001555, respectively, with corresponding $\varepsilon_{Hf}(t)$ values and t_{DM2} ages of −20.93 to + 5.60 and 0.85 Ga to 1.63 Ga.

Eight spots from pyroxene diorite-porphyrite have $^{176}Yb/^{177}Hf$ ratios of 0.021236–0.068351 and $^{176}Lu/^{177}Hf$ ratios of 0.0007767–0.002161. Their corresponding $\varepsilon_{Hf}(t)$ values and t_{DM2} ages range from −1.10 to −8.61 and 1.26 Ga to 1.72 Ga, respectively.

4 Discussion

4.1 Fractional crystallization and assimilative contamination

The diorite-porphyrite and pyroxene diorite-porphyrite samples yield petrographic evidence for alternation (e.g., chlorite alteration; Fig. 2d, e, f, h) and variable loss on ignition (LOI) values of 1.73–2.44 wt% and 2.15–4.71 wt%, respectively. It is, therefore, necessary to evaluate the effect of post-magmatic alteration on elemental mobility. Previous studies have shown that elements including Al, Ti, P, HFSEs, rare earth elements (REEs; excluding Ce and Eu), and transition metals are generally immobile, while Ca, Na, and LILEs are prone to alteration and migration (Polat et al. 2003). Diorite-porphyrite and pyroxene diorite-porphyrite samples exhibit relatively stable contents of Na_2O (3.67–3.93 wt% and 3.31–3.56 wt%, respectively), K_2O (3.00–3.18 wt% and 1.50–2.08 wt%, respectively), and CaO (3.35–3.86 wt% and 4.92–7.05 wt%, respectively). Additionally, the elements Na_2O, K_2O, and CaO exhibit a scattered trend with loss on ignition (LOI) values (Fig. 8a, b, c), indicating that the major elements remain largely immobile. Additionally, Th, Rb, and Ba also show no correlation with LOI (Fig. 8d, e, f), suggesting that LILEs may also be immobile in these samples. In addition, the alteration independent element Zr (Polat et al. 2003) is used to evaluate the effects of alteration on other trace elements, and the overall strong linear relationships indicate weak alteration effects on the elemental characteristics (Fig. 9). Based on the above, alteration has a very limited impact on the whole-rock geochemical composition of the samples in this study. Therefore, for subsequent discussions, major-element contents were recalculated on a 100% volatile-free basis.

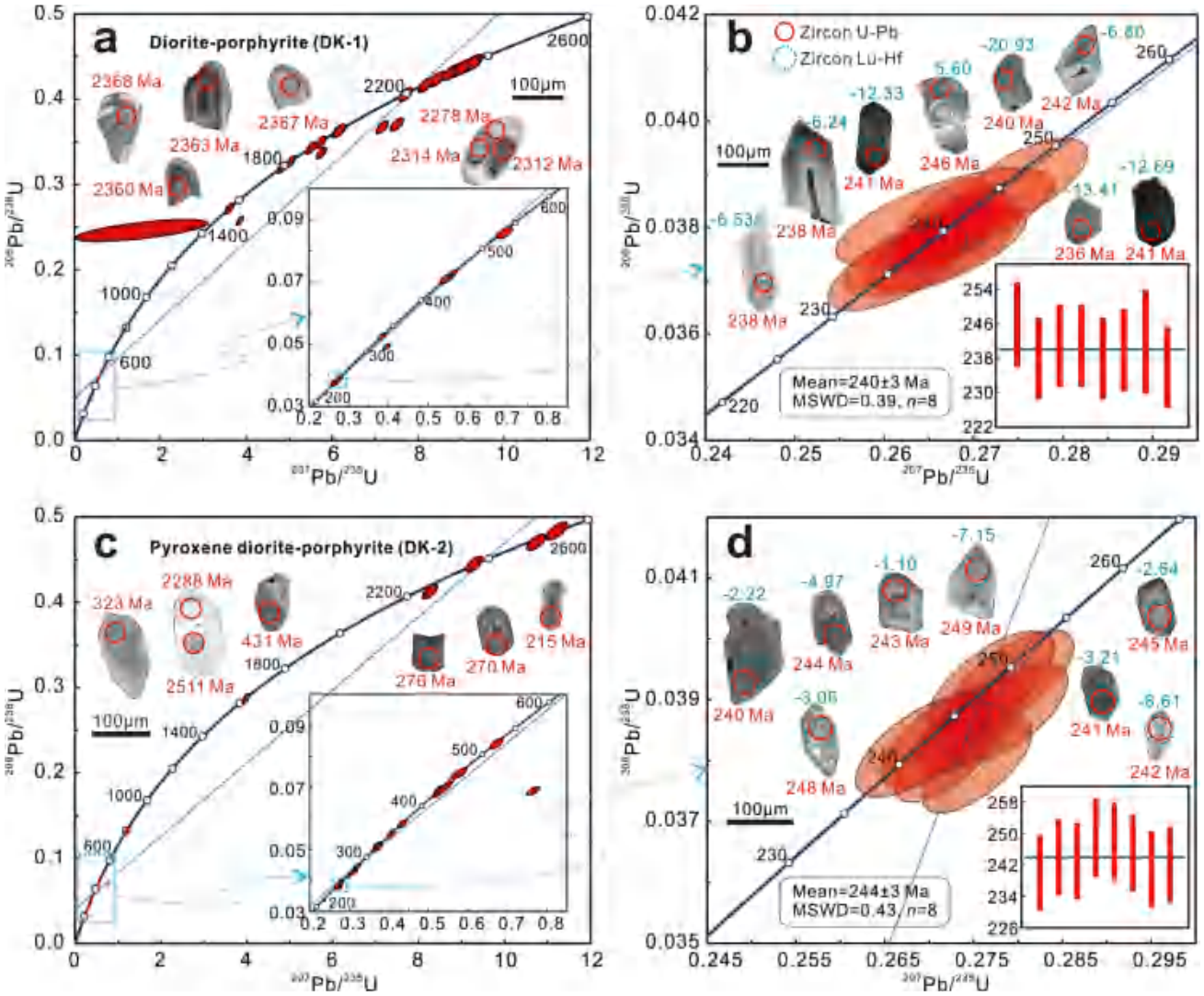

Fig. 4 Cathodoluminescence images of typical zircons, zircon U–Pb concordia diagrams, and age histograms for dioritic rocks in the Dadakenwulashan area of the NQ. MSWD, mean square of weighted deviates. **a** and **b** Diorite-porphyrite (DK-1); **c** and **d** pyroxene diorite-porphyrite (DK-2)

During the upward migration and emplacement of magma from its source region, fractional crystallization and assimilative contamination, or both, typically occur. Therefore, distinguishing whether fractional crystallization and assimilative contamination have occurred is crucial for studying the petrogenesis of rocks. The Dadakenwulashan dioritic rocks from the study area exhibit no obvious linear relationships among MgO and SiO_2, TiO_2, Al_2O_3, Fe_2O_3T, CaO, Cr, and CaO/Al_2O_3 (Fig. 10a-g), indicating that intense fractional crystallization of mafic minerals did not occur during magma evolution. In the chondrite-normalized REE pattern, Eu displays weak negative anomalies to varying degrees (Eu/Eu* = 0.73–0.98). Additionally, a positive correlation between MgO and P_2O_5 is shown in the diagram (Fig. 10g), suggesting the presence of fractional crystallization of plagioclase during magma evolution. The high K/Rb (321–557) ratios also indicate that these diorite-porphyrites have undergone limited evolution, reflecting a rapid ascent process during emplacement without significant crystallization differentiation. Crustal contamination often affects the chemical composition of magmatic rocks, particularly leading to the enrichment of LILEs and LREEs, as well as negative anomalies of Nb, Ta, and Ti and weak positive anomalies of Zr and Hf (Rudnick and Gao 2003). The presence of inherited zircons in zircon dating samples (Fig. 4) and weak positive anomalies of Zr and Hf in the PM-normalized spidergram in this study suggest potential crustal contamination. However, no wall-rock xenoliths were found in the pluton during field investigations, implying

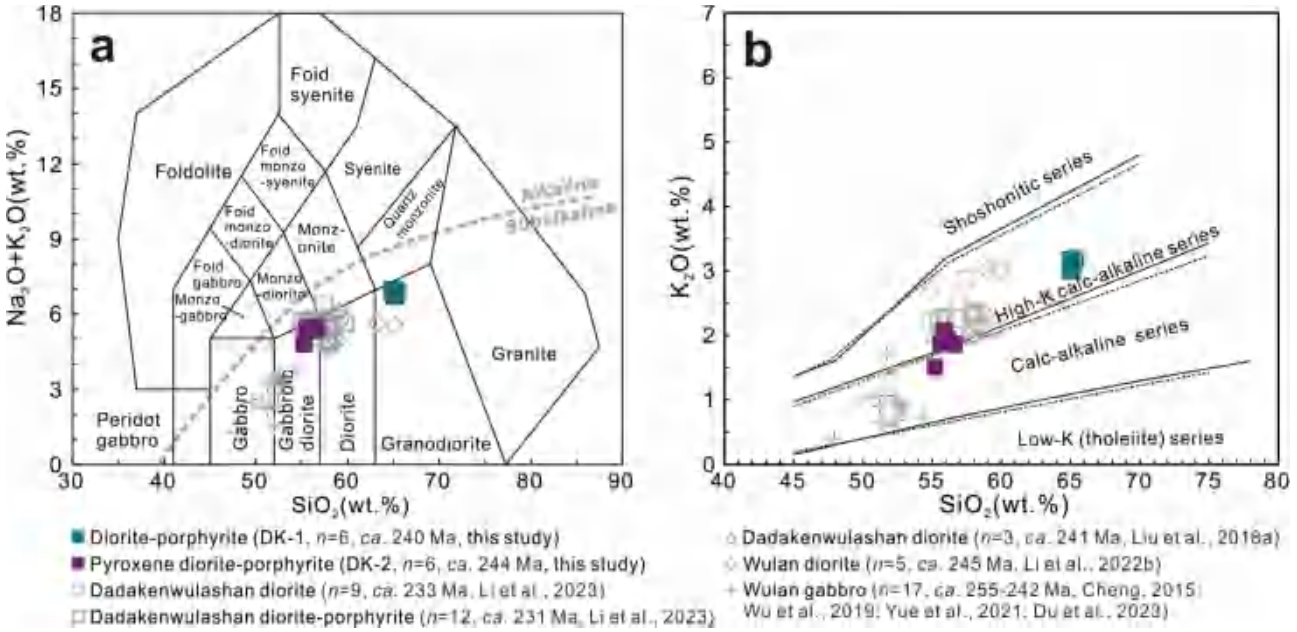

Fig. 5 Geochemical classification diagrams for dioritic rocks in the Dadakenwulashan area of the NQ. **a** Na_2O+K_2O vs. SiO_2 diagram (Middlemost 1994). **b** K_2O versus SiO_2 diagram (Peccerillo and Taylor 1976)

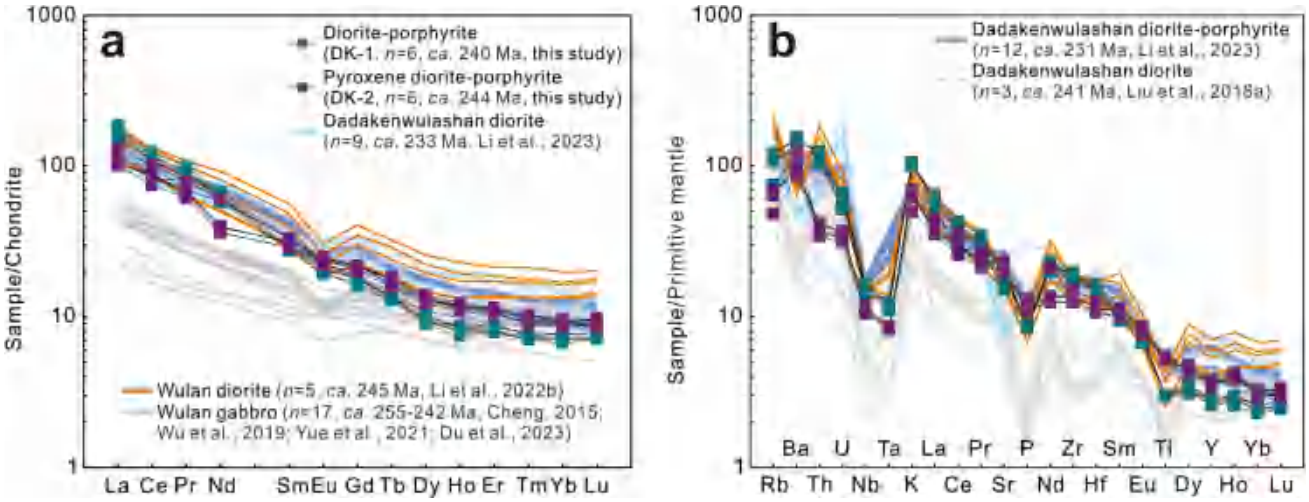

Fig. 6 Chondrite-normalized rare earth element (REE) pattern **a** and primitive mantle (PM)-normalized spidergram **b** for dioritic rocks in the Dadakenwulashan area of the NQ. The values of chondrite and PM are from Sun and McDonough (1989)

that the impact of assimilative contamination may not be significant. Moreover, elements with the same or similar partition coefficients are unaffected by fractional crystallization and partial melting. Therefore, the covariation of these element ratios can be used to analyze whether assimilative contamination has occurred (Campbell and Griffiths 1993). The results show that the La/Yb ratio does not decrease as the Nb/Ta ratio increases (Fig. 10h), indicating limited wall-rock assimilative contamination.

4.2 Petrogenesis of Dadakenwulashan dioritic rocks

The dioritic rocks in this study exhibit similar rare earth element and trace element distribution patterns (Fig. 6), suggesting a certain genetic affinity. Intermediate rocks, including andesite and diorite, are among the most significant rock types at convergent plate margins, and their compositions are usually similar to the average composition of the continental crust (Rudnick and Gao 2003). Therefore, the petrogenesis

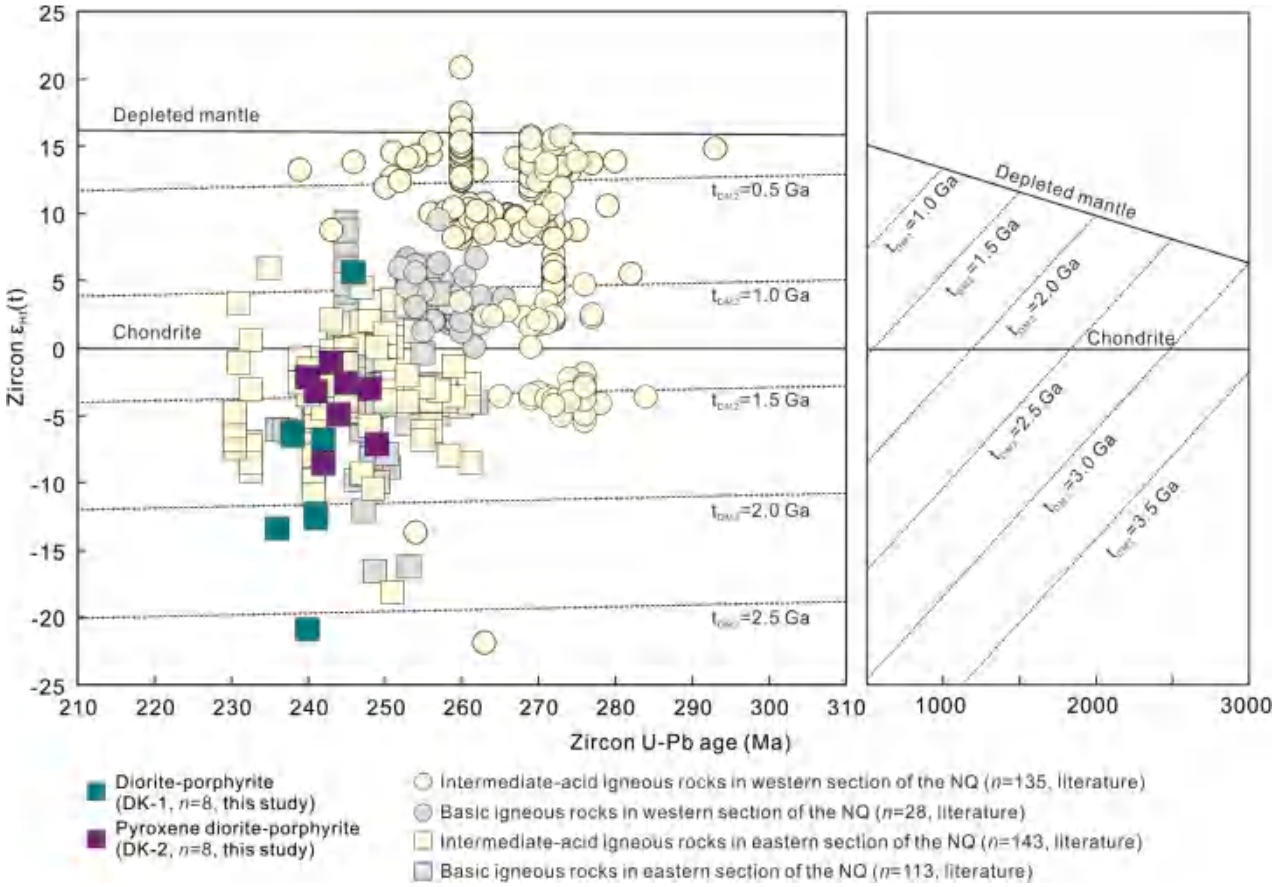

Fig. 7 Zircon $\varepsilon_{Hf}(t)$ vs. zircon U–Pb age diagram for dioritic rocks in the Dadakenwulashan area of the NQ. The literature data of intermediate-acid igneous rocks ($n=135$) in the western NQ are from Dong et al. 2014, 2015; Qiu et al. 2015; Gao et al. 2019; Wang et al. 2023, 2024a; ultrabasic-basic igneous rocks ($n=28$) in the western NQ are from Qian et al. 2018; intermediate-acid igneous rocks ($n=143$) in the eastern NQ are from Zhang 2022; Ding et al. 2022; Li et al. 2022b, 2023; Zheng et al. 2024; basic igneous rocks ($n=113$) in the eastern NQ are from Cheng 2015; Chen et al. 2020; Niu et al. 2018; Yue et al. 2021; Zhang 2022; Li et al. 2022b

of intermediate rocks has been a research hotspot. The main genetic viewpoints include: (1) fractional crystallization of mantle-derived magma (Tatsumi 1982; Grove et al. 2003; Annen et al. 2006; Lee and Bachmann 2014); (2) partial melting of subducted oceanic crust (Defant and Drummond 1990; Kay et al. 1993); (3) partial melting of the mantle wedge metasomatized by subduction fluids or melts (Rogers and Hawkesworth 1989; Kelemen 1995; Carmichael 2002; Parman and Grove 2004); (4) partial melting of the lower crust caused by underplating of mantle-derived magma (Petford and Atherton 1996; Jung et al. 2002); (5) mixing of mantle-derived basaltic magma and crust-derived felsic magma (Clynne 1999; Reubi and Blundy 2009).

Magmatic rocks formed by the crystallization differentiation of mantle-derived magma are characterized by high Cr and Ni concentrations, $Mg^{\#}$ (> 60) values, and low TiO_2 contents (< 0.5 %) (Tatsumi 1982; Grove et al. 2003). However, the dioritic rocks in this study exhibit lower Cr (14.4–42.9 ppm) and Ni (4.86–14.2 ppm) concentrations and $Mg^{\#}$ values (43.1–53.3) and higher TiO_2 contents (0.63–1.19 wt%). Furthermore, since the partition coefficient of La between solid and melt is greater than that of Sm and Yb, the enrichment rate of La in the melt is also higher. This results in an increase in the La/Sm and La/Yb ratios during partial melting (Allègre and Minster 1978). In Fig. 10i, the La/Yb ratios of the samples increases as the La content increases, suggesting that fractional crystallization has a weaker influence on the petrogenesis. This indicates that partial melting is likely the main process of magma evolution in the rocks. Therefore, mantle-derived magma fractional crystallization is not the genetic mechanism of the dioritic rocks in this study.

Partial melting of subducting slab generally produces adakites (Defant and Drummond 1990; McCarron and Smellie 1998). Although the dioritic rocks in this study have low Yb (1.13–1.62 ppm) and Y (11.8–17.3 ppm) concentrations, their variable Sr (319–493 ppm) concentrations, Sr/Y (25.24–33.77) and La/Yb (15.79–35.40)

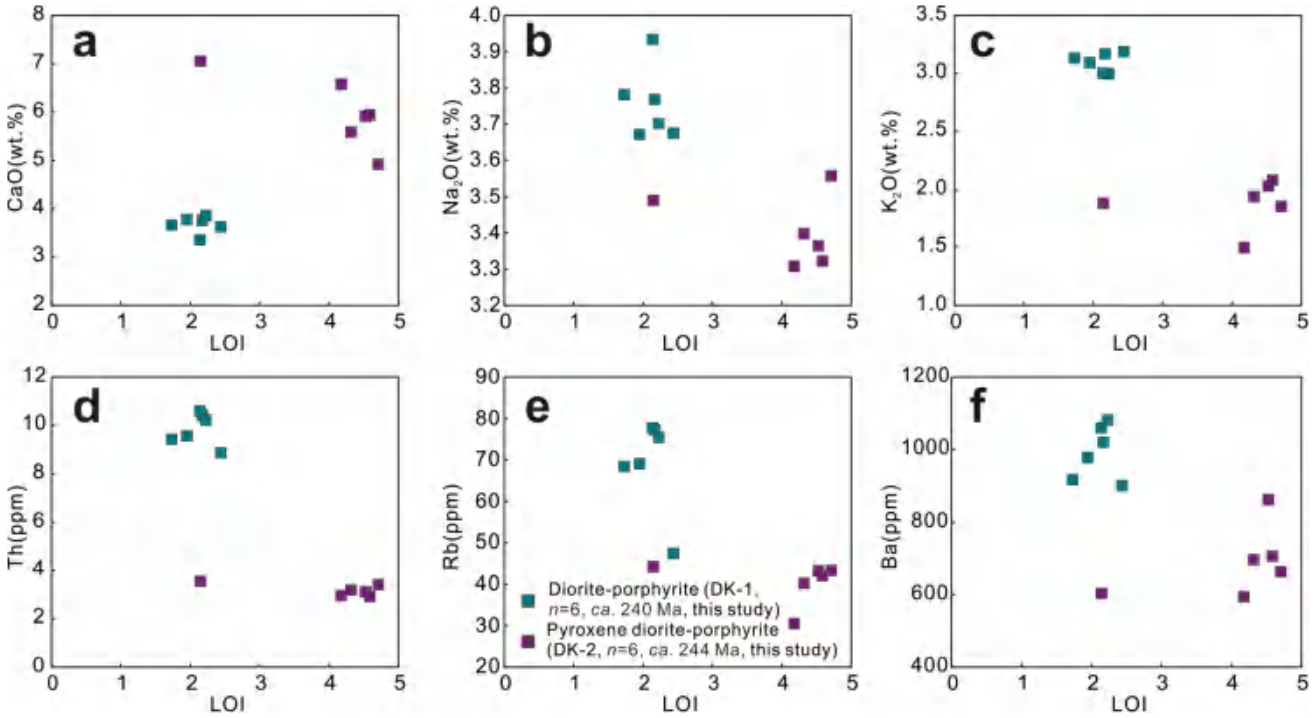

Fig. 8 Bivariate diagrams of selected major oxides and trace elements versus LOI for dioritic rocks in the Dadakenwulashan area of the NQ

ratios and varying degrees of Eu negative anomalies (Eu/Eu* = 0.87–0.97) do not match the geochemical characteristics of typical adakites formed by subducting slab melting (Defant and Drummond 1990). Therefore, their origin of subducting slab partial melting can be excluded (Fig. 11). Melts formed by partial melting of mantle wedge peridotites metasomatized by subducting melts are characterized by high MgO (> 8 wt%) content and low TiO_2 (< 0.5 wt%) content. Melts from partial melting of mantle wedge metasomatized by subducting fluids are characterized by high Sr (> 1000 ppm) and Ba (> 1000 ppm) concentrations and K/Rb (> 1000) ratios (Kelemen 1995). However, the samples have low MgO (1.88–5.16 wt%) content, Sr (< 1000 ppm), Ba (< 1000 ppm) concentrations, and K/Rb (321–557) ratios, as well as high TiO_2 (0.63–1.19 wt%) content, which do not match these characteristics. This indicates that they are not products of partial melting of mantle wedge metasomatized by subduction components.

Experimental petrological studies have shown that melts formed by partial melting of basaltic lower crust generally exhibit low Cr and Ni concentrations, MgO content (< 3 wt%), and $Mg^{\#}$ (< 40) values. Only when mantle material is involved in the petrogenesis can the $Mg^{\#}$ value of the melt exceed 40 (Rapp and Watson 1995). The samples exhibit high Cr (14.4–42.9 ppm) and Ni (4.86–14.2 ppm) concentrations, MgO (1.88–5.16 wt%) content, and $Mg^{\#}$ (43.1–53.3) values. It is evident that partial melting of the mafic lower crust alone can not generate the parental magma of the dioritic rocks studied in this research.

The Nb/Ta (21.2–24.4) and Zr/Hf (42.4–44.7) ratios of the samples are both higher than those of the primitive mantle (Nb/Ta = 17.5 and Zr/Hf = 36.3, Sun and McDonough 1989; Hofmann 1988) and are significantly higher than the average values of the continental crust (Nb/Ta = 12–13 and Zr/Hf = 33, Barth et al. 2000; Taylor and McLennan 1995). Meanwhile, the Rb/Sr (0.07–0.19) and Nd/Th (2.77–7.97) ratios of the samples fall between those of the mantle (Rb/Sr = 0.03 and Nd/Th = 15.0) and the crust (Rb/Sr = 0.35 and Nd/Th = − 3.00) (Taylor and McLennan 1995; Bea et al. 2001), indicating that the source regions of the dioritic rocks in this study may have undergone crust-mantle mixing processes. The zircon Lu–Hf isotope system can effectively record the Hf isotope characteristics of the mixing end-members in magma mixing. The $\varepsilon_{Hf}(t)$ (−20.93 to + 5.60) values (Fig. 9) of the samples exhibit a wide range of variation, suggesting that they may originate from a mixture of mantle- and crust-derived magmas.

The P_2O_5 content in rocks is an important indicator for assessing fractional crystallization and magma mixing (Lee and Bachmann 2014). This is because P_2O_5 primarily exists in apatite, which generally does not crystallize in mafic magmas. As fractional crystallization of other minerals proceeds, the P_2O_5 content in the remaining magma will gradually increase. When apatite begins to crystallize, the P_2O_5 content in the magma will start to decrease, resulting in

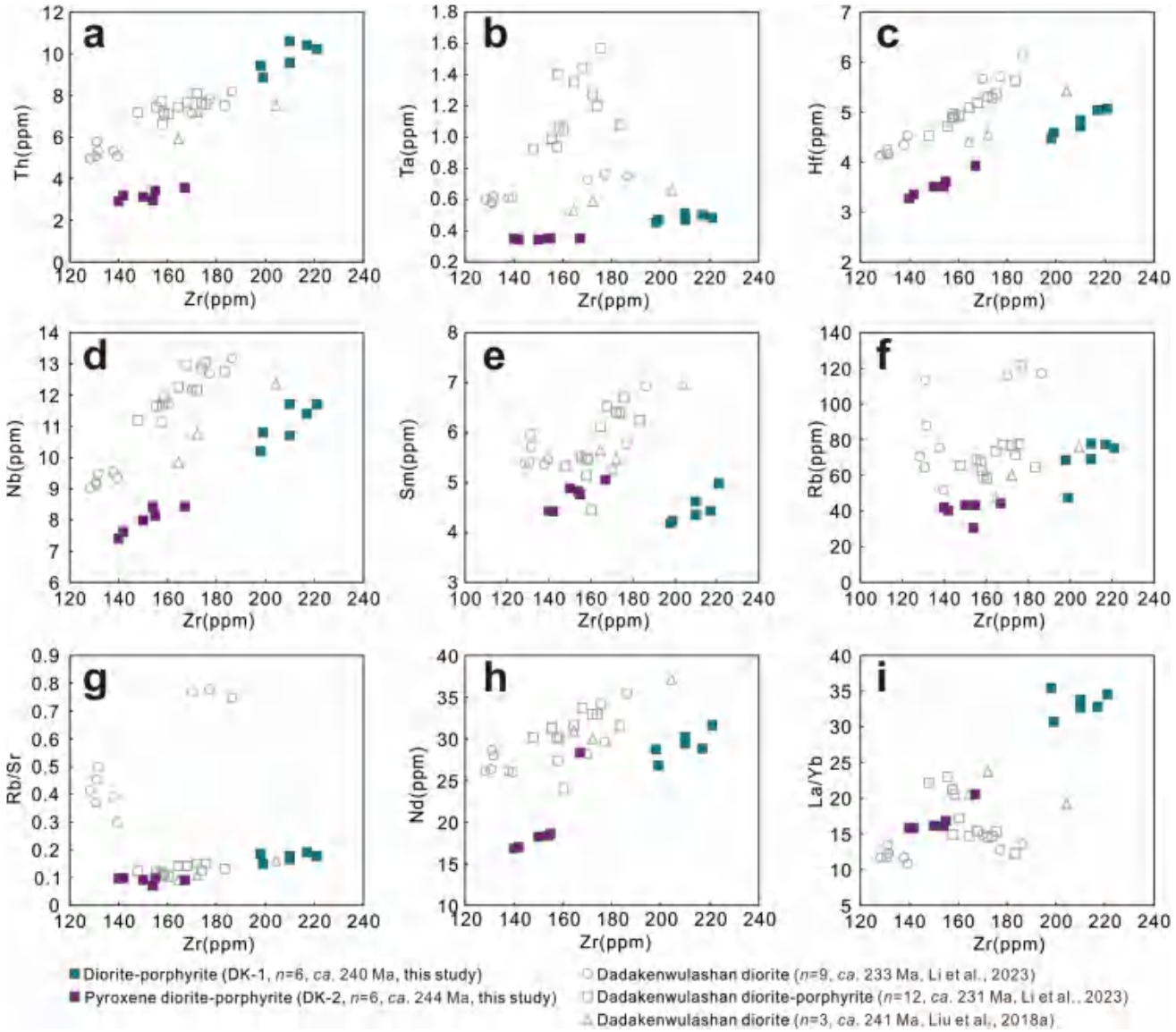

Fig. 9 Bivariate diagrams of selected trace elements and ratios versus Zr for dioritic rocks in the Dadakenwulashan area of the NQ

an upward-bending pattern in the SiO_2 versus P_2O_5 bivariate diagram. Magma mixing will lead to a single linear variation of P_2O_5 content with SiO_2 content. The samples exhibit a trend of magma mixing in the SiO_2 versus P_2O_5 bivariate diagram (Fig. 12a), which is significantly different from the trend of fractional crystallization. The Al_2O_3/MgO versus MgO, Ni versus Cr, and SiO_2/MgO versus Al_2O_3/MgO diagrams (Fig. 12b-d) also indicate that the samples show a clear trend of magma mixing, suggesting that magma mixing is the primary factor in the formation of the dioritic rocks studied in this research.

The magmatic end-members involved in crust-mantle mixing often exhibit significant chemical composition variations. When the already crystallized low-temperature components in the magma (such as felsic magma) encounter high-temperature components (such as mafic magma), they undergo thermal melting and crystal regrowth (Andersson and Eklund 1994), leading to the formation of specific mineral structures such as reverse zoning (D'Lemos 1996). Therefore, the mineral reverse zoning structures developed in intermediate magmatic rocks such as diorite are often regarded as mineralogical indicators of crust-mantle magma interaction (Kuşcu and Floyd 2001). Dioritic rocks in this study exhibit dissolution and complex zoning structures of varying degrees in plagioclase phenocrysts (Fig. 3), and the higher crystallization temperatures of clinopyroxene indicate the involvement of high-temperature mantle-derived components. This further supports that magma mixing is the primary factor in the formation of dioritic rocks in this study. Additionally, previous studies have also shown that mafic

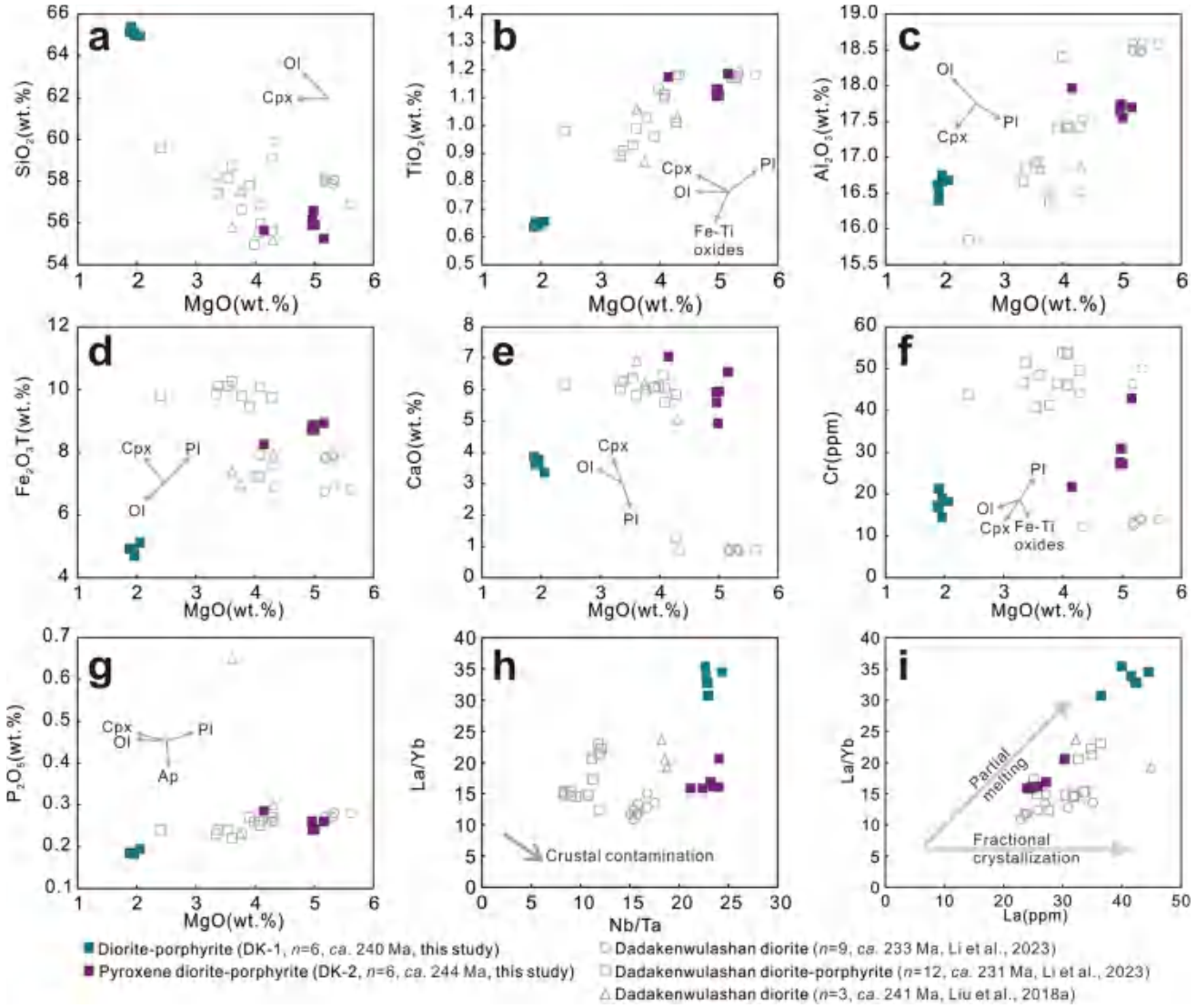

Fig. 10 Harker diagrams **a**–**g**, La/Yb versus Nb/Ta diagram **h**, and La/Yb vs. La diagram **i** for dioritic rocks in the Dadakenwulashan area of the NQ

microgranular enclaves are commonly developed in Permian-Triassic intermediate-acidic rocks in the eastern NQ, which may represent regional basaltic magma underplating and crust-mantle magma mixing (Niu et al. 2018; Li et al. 2022b). Therefore, this study proposes that mantle-derived magma underplating induced the remelting of the ancient amphibolite-facies lower crust, followed by mixing with the underplated basaltic magma, as the formation mechanism of the middle-late Triassic dioritic rocks in the study area.

4.3 Tectonic setting and implications

A significant number of early Late Paleozoic magmatic events related to the post-collisional tectonic system mark the termination of the Wilson cycle related to the Proto-Tethys tectonic evolution. For the Late Paleozoic to Early Mesozoic period, previous studies have proposed six principal tectonic models (as detailed in the Introduction), which can be conceptually grouped into three categories based on their driving mechanisms: (1) subduction-related models (Models 4–6 involving the Buqingshan-A'nimaqing and/or Zongwulong oceanic systems), (2) collision-related models (Models 2–3 addressing continental dynamics), and (3) post-orogenic models (Model 1 concerning orogenic collapse).

In recent years, a large number of Late Paleozoic to Early Mesozoic igneous rocks with arc affinity have been identified in the NQ (Guo et al. 2009; Niu et al. 2018; Wu et al. 2019; Li et al. 2023; Wang et al. 2023, 2024a). Despite frequent magmatic activities during the Late Permian to Early

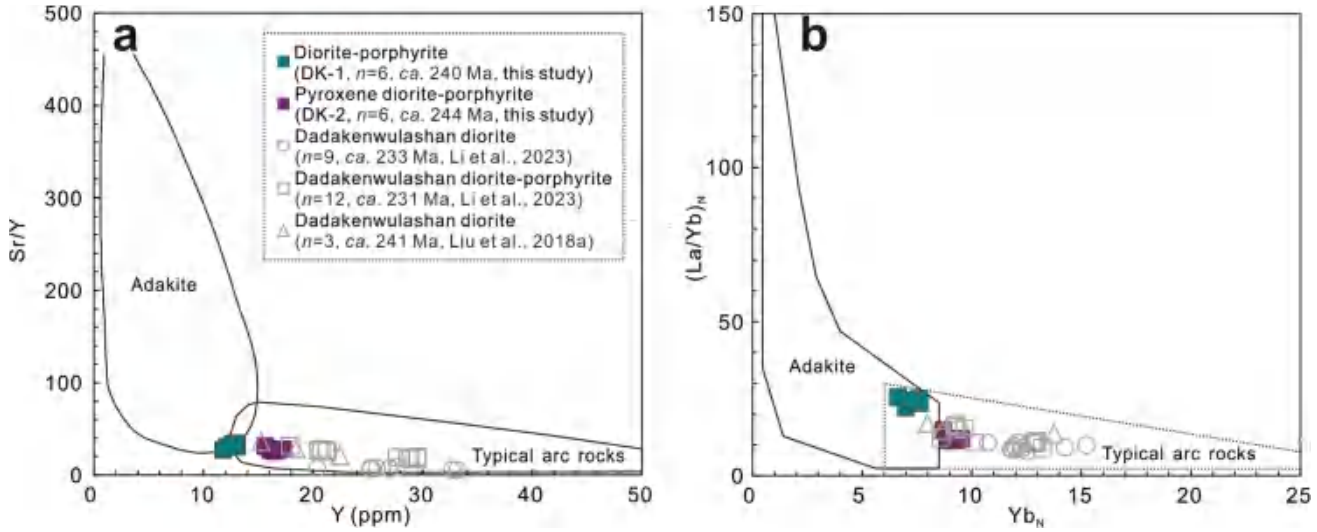

Fig. 11 Diagrams of Sr/Y vs. Y (**a**, Defant and Drummond 1990) and $(La/Yb)_N$ vs. Yb_N (**b**, Defant and Drummond 1990) for dioritic rocks in the Dadakenwulashan area of the NQ

Middle Triassic in the eastern NQ, A-type granites only appeared during the Late Triassic (215–214 Ma; Guo et al. 2009; Chen 2011). In addition, based on the analysis of sedimentary facies and provenance of the Longwuhe Group, previous studies have suggested that it was formed in a forearc basin of an Andean-type active continental margin (Yan et al. 2014). Based on the above evidence, the formation of Late Paleozoic to Early Mesozoic igneous rocks in the NQ is unrelated to models such as late collisional orogenic to post-orogenic extension, intracontinental subduction, and oblique collision of the West Qinling Block with the Qaidam Block.

Some scholars believe that there is no complete subduction and closure tectonic–magmatic cycle of the Paleo-Tethys Ocean in the NQ, mainly based on the negation of the ophiolite assemblage identified in the Tianjunnanshan area of the eastern section of the Zongwulong Tectonic Belt, which consists of ultramafic rocks, gabbro, basalt, basic dykes, and siliceous rocks (Wang et al. 2001; Guo et al. 2009). This is because not only a zircon U–Pb age of 318 ± 3 Ma (Wang et al. 2001) but also a zircon U–Pb age of 509 ± 4 Ma (Fu et al. 2021) was obtained from it. Therefore, some scholars have questioned the zircon U–Pb age of 318 ± 3 Ma (Wang et al. 2001) and believe that the ophiolite was formed in the Early Paleozoic, representing remnants of the Proto-Tethys ocean basin. However, in recent years, ophiolite fragments consisting of diabase, gabbro, spilite, pillow basalt, and siliceous rocks have also been discovered in the Zongwulongshan area of the western section of the Zongwulong Tectonic Belt, and a U–Pb isotopic age of 300.7 ± 1.4 Ma was obtained for the pillow basalt (Xu et al. 2019). This further supports the existence of ophiolites in the Zongwulong Tectonic Belt during the Late Paleozoic. In addition, some scholars believe that the Late Paleozoic to Early Mesozoic magmatic activities in the NQ were formed by the northward subduction of the Buqingshan-A'nimaqing Ocean, based on comparisons of magmatic activities between the eastern NQ and the East Kunlun Tectonic Belt. However, this view largely ignores the extensive magmatic activity in the western NQ (Li et al. 2023). In view of this, the authors of this paper have previously summarized in detail the distribution characteristics and magmatic activities of igneous rocks in the NQ and the East Kunlun Tectonic Belt and found significant differences (Wang et al. 2024a). Additionally, if the northward subduction of the Buqingshan-A'nimaqing Ocean in the southern Qaidam were responsible, one would expect a significant distribution of igneous rocks from this period in the Northern Qaidam Tectonic Belt, closer to the ocean. However, the reality is that Carboniferous to Triassic igneous rocks in the NQ are predominantly distributed in the Zongwulong Tectonic Belt and the Oulongbuluke Block, with few occurrences in the Northern Qaidam Tectonic Belt. Furthermore, no reports of magmatic rocks from this period have been found in the South Qilian region. Additionally, previous studies have identified typical Middle Permian O-type adakites in the Yanchangbeishan area of the western NQ (Qiu et al. 2015; Wang et al. 2024a), which supports the melting of a young and hot subducting slab in the NQ and further indicates the existence of an ocean basin with subduction and consumption processes.

The Zongwulong Tectonic Belt in the NQ preserves a series of ductile shear zones and thrust faults (Gao et al. 2021). By analyzing the foliation and lineation of these ductile shear zones, combined with microscopic observations of mineral deformation characteristics, it has been determined that the shear deformation is dominated by NEE-SWW-trending thrust-strike-slip kinematics (Gao et al. 2021). This

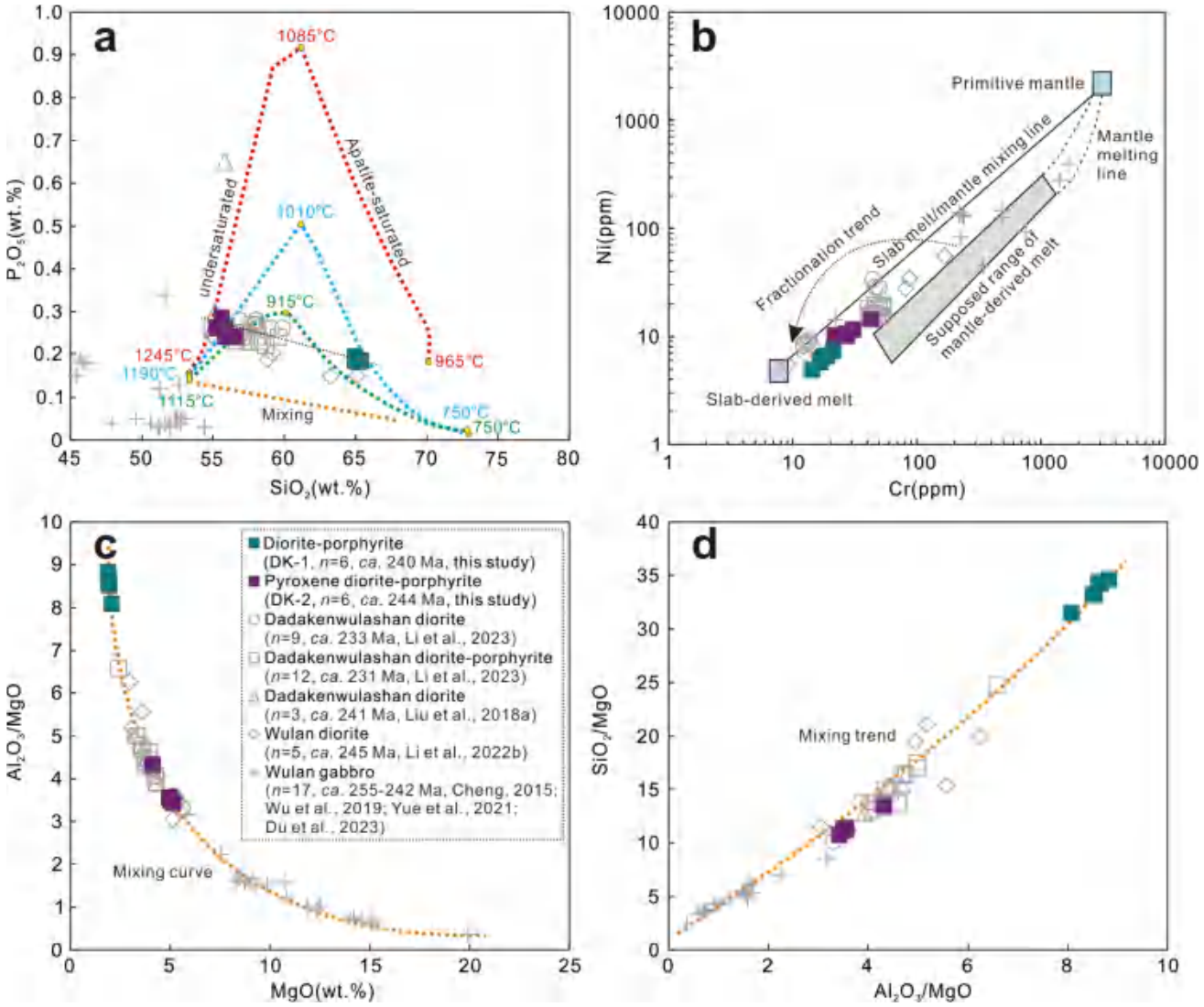

Fig. 12 Diagrams of P_2O_5 versus SiO_2 (**a**, Lee and Bachmann 2014), Ni vs. Cr **b**, Al_2O_3/MgO vs. MgO **c**, and SiO_2/MgO versus Al_2O_3/MgO **d** for dioritic rocks in the Dadakenwulashan area of the NQ

suggests an oblique collision between the Oulongbuluke Block and the South Qilian, clearly recording the subduction-collision process of the local oceanic basin rather than a far-field effect (Gao et al. 2021). During the Carboniferous, the NQ was dominated by shallow marine sedimentation, depositing the Tuergendaban Formation (phyllite interbedded with marble and metavolcanic rocks), with protoliths consisting of clastic-carbonate assemblages (Sun et al. 2014). The region is characterized by Carboniferous extensional rift flysch deposits and Lower Permian passive continental margin carbonate deposits (Peng 2015), collectively forming a forearc system that evolved into an accretionary wedge after closure (Zhao et al. 2020). In the Early Permian, marine transgression intensified, leading to an increase in carbonate deposition and the formation of the Guokeshan Formation (limestone, banded limestone interbedded with clastic rocks), reflecting a stable passive continental margin environment (Zhang 2017). From the Late Permian to Middle Triassic, shallow marine carbonate-clastic sequences were deposited, containing abundant limestone gravels, indicating a tectonic transition from a passive to an active margin (Peng 2015). The Permian Ganjia Formation contains pillow lavas interbedded with marine sediments, while the Triassic Longwuhe Formation consists of volcanic-bearing deep-sea turbidites, suggesting that the Zongwulong remnant oceanic basin persisted until the Middle-Late Triassic. This basin may have been connected to the Shangdan Belt in the West Qinling via the Qinghai Lake South Mountain (Guo et al. 2009).

Based on the above analysis, it can be seen that the tectonic-magmatic events in the Late Paleozoic to Early Mesozoic in the NQ were complex geological processes. Despite

different views, increasing evidence suggests the existence of the Zongwulong Paleo-Tethys Ocean in the NQ, with a complete process of ocean basin development, subduction and consumption, and collision and closure (Wang et al. 2023, 2024a).

The dioritic rocks in the study exhibit negative anomalies of Nb, Ta, and Ti, a characteristic similar to island arc igneous rocks, which is further supported by the Rb−Yb + Ta diagram (Fig. 13a). The co-occurrence of intermediate-mafic plutons and dikes typically indicates the emplacement of deep-source magmas into different crustal levels along fractures, a process often closely associated with regional extensional tectonics (Khan et al. 2007; French and Heaman 2010). In the Dadakenwulashan area, the widely exposed dioritic dikes often appear in parallel arrangements (Fig. 1c), forming large-scale dike swarms, which can thus be regarded as a prominent indicator of regional extension. Intermediate-mafic dikes related to lithospheric extension can form in various tectonic settings, such as intracontinental rifts, mantle plumes, or back-arc basins, where basaltic magma fills tensional fractures. No contemporaneous mantle plume activity has been recorded in the NQ, making a sudden change in the tectonic setting within an extremely short timeframe unlikely. Instead, numerous geological records point to a back-arc extensional setting (Cai et al. 2019; Sun et al. 2022), such as the Middle Triassic alkaline volcanic-intrusive complex system in the eastern NQ (Cai et al. 2019; unpublished data in this paper). Additionally, the high Ti/V ratios (40.4–60.0) of the dioritic rocks in the study area also suggest a back-arc extensional setting (Shervais 1982), consistent with the clinopyroxene composition in the pyroxene diorite-porphyrite, indicating a back-arc setting (Fig. 13b). Therefore, the dioritic rocks in Dadakenwula Mountain were likely formed in a back-arc extensional setting along an active continental margin subduction zone.

The specific process of diorite-porphyrite and pyroxene diorite-porphyrite formation is as follows: With the continuous subduction of the Zongwulong Paleo-Tethys Ocean, a series of subduction-related Late Paleozoic magmatism (318–252 Ma) formed in the western NQ (Wang et al. 2024a, 2025). The Buqingshan-A'nimaqing Ocean began to subduct northward at ca. 270 Ma (Dong et al. 2018). Mantle convection and continuous subduction resulted in an increase in the subduction slab angle, thereby initiating roll-back of the Zongwulong Paleo-Tethys subduction slab (Wang et al. 2024a). Induced by the slab rollback, the Zongwulong Paleo-Tethys subduction zone gradually retreated obliquely. The emergence of Xuji diorite (Chen et al. 2020) indicates that the Zongwulong Paleo-Tethys subduction zone had retreated to the eastern NQ by ca. 258 Ma. With the continued roll-back of the subduction slab, the tectonic stress in some areas of the eastern NQ gradually transitioned from compression to extension, providing sufficient space for the upwelling of deep asthenospheric mantle. This intensified mantle-derived magma underplating, and under the action of releasing a large amount of heat, the ancient lower crust began to remelt. Magma mixing gradually increased, forming a series of continental arc igneous rocks with negative $\varepsilon_{Hf}(t)$ values (Fig. 9) containing mafic microgranular enclaves in the

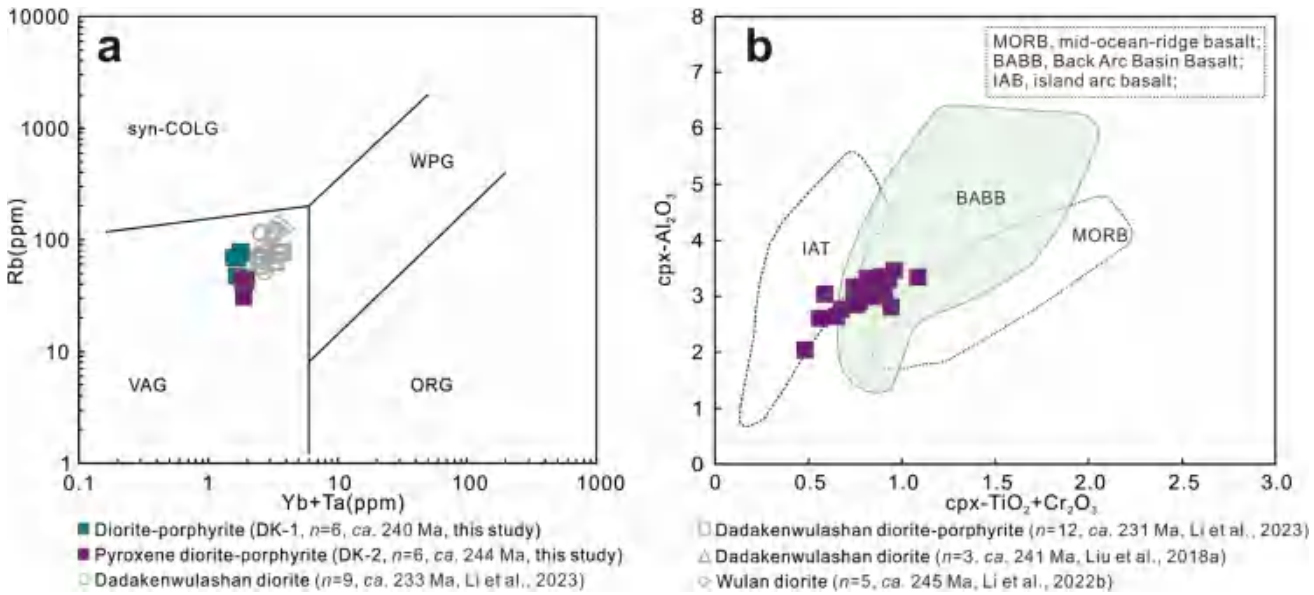

Fig. 13 Diagrams of Rb vs. Yb + Ta (**a**, Pearce et al. 1984) and cpx-Al_2O_3 vs. cpx-$TiO_2 + Cr_2O_3$ **b** for the studied igneous rocks of the NQ

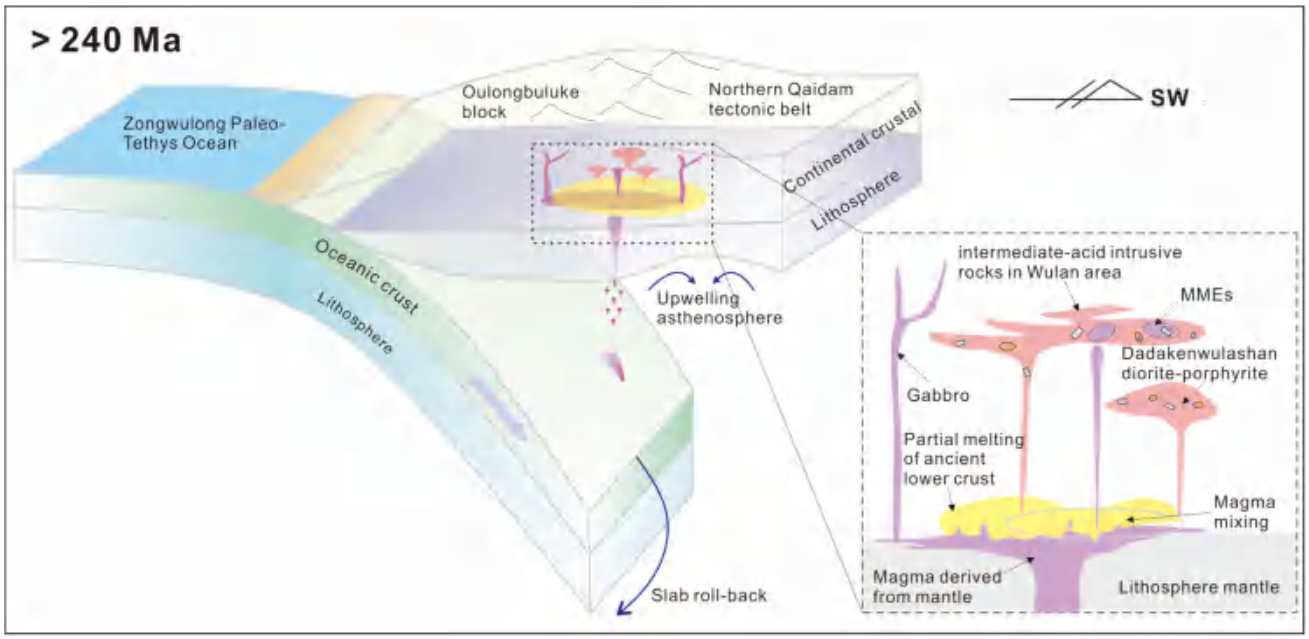

Fig. 14 Schematic tectonic cartoon showing the subduction of the Zongwulong Paleo-Tethys Ocean in the NQ

Wulan area of the NQ (Niu et al. 2018; Li et al. 2022b). Additionally, in the back-arc extension setting, the diorite-porphyrite and pyroxene diorite-porphyrite in this study intruded and emplaced (Fig. 14).

5 Conclusions

(1) LA-ICP-MS zircon U–Pb dating indicates that diorite porphyrite and pyroxene diorite porphyrite formed in the Middle Triassic (244–240 Ma).
(2) Comprehensive analysis of petrography, mineralogy, geochemistry, and zircon Hf isotopes indicates that the dioritic rocks in the Dadakenwulashan were formed through magma mixing following the melting of ancient lower crust induced by mantle-derived magma underplating.
(3) The underplating of mantle-derived melts and the crust-mantle magma mixing dominated the eastern NQ crustal reworking during slab roll-back of the subducted Zongwulong Paleo-Tethys Ocean.

Acknowledgements Prof. Shiping He provided guidance during the fieldwork; Drs. Yanguang Li, Shuangshuang Wang, Mengqi Jin, and Ningchao Zhou provided laboratory help; We sincerely thank all participants. This research was financially supported by China Geological Survey Project (DD20190069 and DD20221636) and Science and Technology Plan Project in Shaanxi Province, China (2023-JC-ZD-14, 2023-JC-YB-236, 2024JC-YBQN-0249, and 2022JQ-286).

Author contributions Panlong Wang: Conceptualization, investigation, writing original draft, formal analysis, writing-review & editing; Yongjun Li: Conceptualization, writing-review & editing; Yujun Zhuang: Conceptualization, investigation; Pingyang Gu: Conceptualization, investigation; Chao Shi: investigation; Jiaxin Yan: investigation; Gaoxue Yang: Conceptualization, writing—review & editing; Wei Li: Formal analysis; Hai Li: Formal analysis; Jianye Zhang: Formal analysis; Hao Fu: Formal analysis.

Funding China Geological Survey, Ministry of Natural Resources (DD20190069, DD20221636), Natural Science Foundation of Shaanxi Province (2023-JC-ZD-14, 2023-JC-YB-236, 2024JC-YBQN-0249, 2022JQ-286).

Declarations

Competing interest The authors declare that they have no known competing financial interests or personal relationships that could have appeared to influence work reported in this paper.

References

Allègre CJ, Minster JF (1978) Quantitative models of trace element behavior in magmatic processes. Earth Planet Sci Lett 38(1):1–25. https://doi.org/10.1016/0012-821X(78)90123-1

Allen MB, Song SG, Wang C, Zeng RY, Wen T (2023) An oblique subduction model for closure of the Proto-Tethys and Palaeo-Tethys oceans and creation of the Central China Orogenic Belt. Earth Sci Rev 240:104385. https://doi.org/10.1016/j.earscirev.2023.104385

Andersson UB, Eklund O (1994) Cellular plagioclase intergrowths as a result of crystal-magma mixing in the Proterozoic Åland rapakivi

batholith, SW Finland. Contrib Mineral Petrol 117(2):124–136. https://doi.org/10.1007/BF00286837

Annen C, Blundy JD, Sparks RSJ (2006) The genesis of intermediate and silicic magmas in deep crustal hot zones. J Petrol 47(3):505–539

Barth MG, McDonough WF, Rudnick RL (2000) Tracking the budget of Nb and Ta in the continental crust. Chem Geol 165(3–4):197–213. https://doi.org/10.1016/S0009-2541(99)00173-4

Bea F, Arzamastsev A, Montero P, Arzamastseva L (2001) Anomalous alkaline rocks of Soustov, Kola: evidence of mantle-derived metasomatic fluids affecting crustal materials. Contrib Mineral Petrol 140(5):554–566. https://doi.org/10.1007/s004100000211

Cai PJ, Zhang Y, Xu RK, Zheng YY, Guo XZ, Chen X (2019) Zircon U–Pb geochronology, geochemistry, and Sr–Nd isotopes of Shuangkoushan quartz-syenite, northern Qaidam China. Geotecton Metallog 43(2):322–338. https://doi.org/10.16539/j.ddgzyckx.2019.02.011

Cai PJ, Chen X, Majka J, Klonowska I, Jeanneret P, Xu RK, Zheng YY (2021) Two stages of crust-mantle interaction during oceanic subduction to continental collision: insights from mafic-ultramafic complexes in the North Qaidam orogen. Gondwana Res 89:247–264. https://doi.org/10.1016/j.gr.2020.08.018

Campbell IH, Griffiths RW (1993) The evolution of the mantle's chemical structure. Lithos 30(3–4):389–399. https://doi.org/10.1016/0024-4937(93)90047-G

Carmichael IS (2002) The andesite aqueduct: Perspectives on the evolution of intermediate magmatism in west-central (105–99° W) Mexico. Contrib Mineral Petrol 143(6):641–663. https://doi.org/10.1007/s00410-002-0370-9

Chen J (2011) Geochemical characteristics and tectonic significance of intermediate-acid intrusive rocks in Shengge Area, Wulan County, Qinghai Province. Changan University, Changan

Chen NS, Gong SL, Sun M, Li XY, Xia XP, Wang QY, Wu FY, Xu P (2009) Precambrian evolution of the Quanji Block, northeastern margin of Tibet: insights from zircon U–Pb and Lu–Hf isotope compositions. J Asian Earth Sci 35(3–4):367–376. https://doi.org/10.1016/j.jseaes.2008.10.004

Chen XH, Gehrels G, Yin A, Li L, Jiang RB (2012a) Paleozoic and Mesozoic basement magmatisms of eastern Qaidam basin, northern Qinghai-Tibet Plateau: LA-ICP-MS zircon U–Pb geochronology and its geological significance. Acta Geol Sin (Eng) 86(2):350–369. https://doi.org/10.1111/j.1755-6724.2012.00665.x

Chen NS, Zhang L, Sun M, Wang QY, Kusky TM (2012b) U–Pb and Hf isotopic compositions of detrital zircons from the paragneisses of the Quanji Massif, NW China: implications for its early tectonic evolutionary history. J Asian Earth Sci 54:110–130. https://doi.org/10.1016/j.jseaes.2012.04.006

Chen M, Xue CJ, Xue WW, Zhao WT (2020) Discovery and geological significance of Xuji diorite in Zongwulong tectonic belt on the northern margin of Qaidam Basin. Acta Petrol Mineral 39(5):552–568

Cheng TT (2015) Zircon U–Pb dating and tectonic setting of intrusive rocks in Wulan along the North Margin of Qaidam Terrane. Hefei University of Technology, Hefei

Cheng F, Jolivet M, Hallot E, Zhang DW, Zhang CH, Guo ZJ (2017) Tectono-magmatic rejuvenation of the Qaidam craton, northern Tibet. Gondwana Res 49:248–263. https://doi.org/10.1016/j.gr.2017.06.004

Clynne MA (1999) A complex magma mixing origin for rocks erupted in 1915, Lassen Peak, California. J Petrol 40(1):105–132

D'Lemos RS (1996) Mixing between granitic and dioritic crystal mushes, Guernsey, Channel Islands, UK. Lithos 38(3–4):233–257. https://doi.org/10.1016/0024-4937(96)00007-2

Defant MJ, Drummond MS (1990) Derivation of some modern arc magmas by melting of young subducted lithosphere. Nature 347:662–665. https://doi.org/10.1038/347662a0

Ding QF, Pan T, Zhou X, Cheng L, Li SP, Han J, Qian Y, Gao Y, Shang MY (2022) Geochronology, petrogenesis, and tectonic significance of the granites in the Chaqiabeishan area of the Quanji Massif, northwestern China. Geol J 57(3):1241–1261. https://doi.org/10.1002/gj.4338

Dong ZC, Xiao PX, Gu PY, Zhang HD, Chen RM, Zha XF (2014) Geochronology, geochemistry and Hf isotope characteristics of Yanchangbeishan granodiorite of Lenghu area in Qinghai. Northwest Geol 47(4):141–155

Dong ZC, Yang C, Gu PY, Wang H, Zha XF, Chen RM, Zhang HD (2015) Geochronology and geochemistry of Yanchangbeishan biotite adamellite of Lenghu area in Qinghai and their geological significance. Geotecton Metallog 39(1):167–178. https://doi.org/10.16539/j.ddgzyckx.2015.01.005

Dong YP, He DF, Sun SS, Liu XM, Zhou XH, Zhang FF, Yang Z, Cheng B, Zhao GC, Li JH (2018) Subduction and accretionary tectonics of the East Kunlun orogen, western segment of the Central China orogenic system. Earth Sci Rev 186:231–261. https://doi.org/10.1016/j.earscirev.2017.12.006

Dong YP, Sun SS, Santosh M, Zhao J, Sun JP, He DF, Shi XH, Hui B, Cheng C, Zhang GW (2021) Central China orogenic belt and amalgamation of east Asian continents. Gondwana Res 100:131–194. https://doi.org/10.1016/j.gr.2021.03.006

Du W, Pei L, Li RB, Li ZC, Liu CJ, Wang M, Lin H, Pei XZ (2023) Zircon U–Pb dating and geochemical characteristics of Chahannuo gabbros in the northern margin of Qaidam basin, northern Tibetan Plateau. Minerals 13(5):651. https://doi.org/10.3390/min13050651

French JE, Heaman LM (2010) Precise U–Pb dating of Paleoproterozoic mafic dyke swarms of the Dharwar craton, India: implications for the existence of the Neoarchean supercraton Sclavia. Precambrian Res 183(3):416–441. https://doi.org/10.1016/j.precamres.2010.05.003

Fu CL, Yan Z, Xiao WJ, Wang BZ, Niu ML, Li XC, Yu LJ (2021) Identification and geological significance of the early Paleozoic Tianjunnanshan remnant ocean basin in the Zongwulong belt, NE Tibetan Plateau. Acta Petrol Sin 37(8):2401–2418

Fu CL, Yan Z, Aitchison JC, Xiao WJ, Buckman S, Wang BZ, Zhai QG, Cao B (2022) Short-lived intra-oceanic arc-trench system in the North Qaidam belt (NW China) reveals complex evolution of the Proto-Tethyan Ocean. GSA Bull 134(7–8):1741–1759. https://doi.org/10.1130/b36127.1

Fu CL, Yan Z, Aitchison JC, Xiao WJ, Buckman S, Wang BZ (2024) Subduction within the Proto-Tethys Ocean revealed by recognition of the earliest Phanerozoic intra-oceanic arc, northern Tibetan Plateau. Earth Space Sci 11(3):e2023EA002985. https://doi.org/10.1029/2023ea002985

Gao WL, Wang ZX, Li LL, Cui MM, Qian T, Hu JJ (2019) Discovery of the Permian granite in Saishiteng mountain of the northern Qaidam basin and its tectonic significance. Acta Geol Sin 93(4):816–829. https://doi.org/10.19762/j.cnki.dizhixuebao.2019101

Gao WL, Wang ZX, Li LL, Qian T, Cui MM (2021) $^{40}Ar/^{39}Ar$ laser dating of the Zongwulong ductile shear zone in northeastern Tibetan Plateau: constraints on the time of Indosinian orogeny. Geol China 48(1):149–160

Gehrels GE, Yin A, Wang XF (2003) Magmatic history of the northeastern Tibetan Plateau. J Geophys Res 108(B9):2002jb001879. https://doi.org/10.1029/2002jb001876

Grove TL, Elkins-Tanton LT, Parman SW, Chatterjee N, Müntener O, Gaetani GA (2003) Fractional crystallization and mantle-melting controls on calc-alkaline differentiation trends.

Contrib Mineral Petrol 145(5):515–533. https://doi.org/10.1007/s00410-003-0448-z

Guo AL, Zhang GW, Qiang J, Sun YG, Li G, Yao AP (2009) Indosinian Zongwulong orogenic belt on the northeastern margin of the Qinghai-Tibet plateau. Acta Petrol Sin 25(1):1–12

Hofmann AW (1988) Chemical differentiation of the Earth: The relationship between mantle, continental crust, and oceanic crust. Earth Planet Sci Lett 90(3):297–314. https://doi.org/10.1016/0012-821X(88)90132-X

Jung S, Hoernes S, Mezger K (2002) Synorogenic melting of mafic lower crust: constraints from geochronology, petrology and Sr, Nd, Pb and O isotope geochemistry of quartz diorites (Damara orogen, Namibia). Contrib Mineral Petrol 143(5):551–566. https://doi.org/10.1007/s00410-002-0366-5

Kay SM, Ramos VA, Marquez M (1993) Evidence in Cerro Pampa volcanic rocks for slab-melting prior to ridge-trench collision in southern south America. J Geol 101(6):703–714. https://doi.org/10.1086/648269

Kelemen PB (1995) Genesis of high Mg# andesites and the continental crust. Contrib Mineral Petrol 120(1):1–19. https://doi.org/10.1007/BF00311004

Khan T, Murata M, Karim T, Zafar M, Ozawa H, Hafeez-ur-Rehman (2007) A cretaceous dike swarm provides evidence of a spreading axis in the back-arc basin of the Kohistan paleo-island arc, northwestern Himalaya Pakistan. J Asian Earth Sci 29(2–3):350–360. https://doi.org/10.1016/j.jseaes.2006.04.001

Kuşcu GG, Floyd PA (2001) Mineral compositional and textural evidence for magma mingling in the Saraykent volcanics. Lithos 56(2–3):207–230. https://doi.org/10.1016/S0024-4937(00)00051-7

Lee CA, Bachmann O (2014) How important is the role of crystal fractionation in making intermediate magmas? Insights from Zr and P systematics. Earth Planet Sci Lett 393:266–274. https://doi.org/10.1016/j.epsl.2014.02.044

Li WY (2024) The Paleo-Tethys tectonic evolution and corresponding metallogenesis. Acta Geol Sin 98(11):3255–3273. https://doi.org/10.19762/j.cnki.dizhixuebao.2024404

Li C, Niu ML, Yuan XY, Yan Z, Wu Q, Li XC, Sun Y (2022a) Geochemical signals of coexisting magma mixing and fractional crystallization processes in the arc setting: case study of Wulan intrusive suite in the NE Tibet Plateau. Lithos 432:106914. https://doi.org/10.1016/j.lithos.2022.106914

Li XC, Niu ML, Yan Z, Yakymchuk C, Fu CL, Li C, Sun Y, Wu Q, He JH (2022b) Early Paleozoic continental arc mafic magmatism in the north Qaidam tectonic belt: implications for subduction of the proto-Tethyan oceanic lithosphere. Lithosphere 2022(1):3011662. https://doi.org/10.2113/2022/3011662

Li HR, Qian Y, Sun FY, Wang YZ (2023) Paleozoic to Mesozoic magmatism in north Qaidam, Qinghai Province, NW China: implications for tectonic evolution. Gondwana Res 115:37–56. https://doi.org/10.1016/j.gr.2022.11.011

Li J, Wu C, Li XG, Zuza AV, Haproff PJ, Zhao YH, Zhao WT, Yue YH, Ding L (2024) Tectonic inversion of an intracontinental rift basin: An example from the opening and closure of the Paleo-Tethys Ocean, northern Tibetan Plateau. Geol Soc Am Bull 136(11–12):5145–5173. https://doi.org/10.1130/b37605.1

Liu YL, Liu ZG, Zhang AK, He SY, Zhang DM, Mao SY, Li XL, Kui MJ (2018a) LA-ICP-MS zircon U–Pb age and petrogeochemical characteristics of diorite from Dadakenwulashan area on the northern margin of Qaidam basin and their tectonic implications. Miner Depos 37(5):1079–1090. https://doi.org/10.16111/j.0258-7106.2018.05.011

Liu YJ, Liu CL, Ren ZB, Jia YH, Zhang KH (2018b) Deep prospecting prediction of the Dadakenwulashan lead-zinc deposit in Qinghai by using primary halo method. Northwest Geol 51(1):238–246

Lu SN, Li HK, Zhang CL, Niu GH (2008) Geological and geochronological evidence for the Precambrian evolution of the Tarim Craton and surrounding continental fragments. Precambrian Res 160(1–2):94–107. https://doi.org/10.1016/j.precamres.2007.04.025

McCarron JJ, Smellie JL (1998) Tectonic implications of fore-arc magmatism and generation of high-magnesian andesites: Alexander Island, Antarctica. J Geol Soc 155(2):269–280. https://doi.org/10.1144/gsjgs.155.2.0269

Metcalfe I (2021) Multiple Tethyan ocean basins and orogenic belts in Asia. Gondwana Res 100:87–130. https://doi.org/10.1016/j.gr.2021.01.012

Middlemost EAK (1994) Naming materials in the magma/igneous rock system. Earth Sci Rev 37(3–4):215–224. https://doi.org/10.1016/0012-8252(94)90029-9

Morimoto N (1988) Nomenclature of pyroxenes. Miner Petrol 39(1):55–76. https://doi.org/10.1007/BF01226262

Niu ML, Zhao QQ, Wu Q, Li XC, Yan Z, Li JL, Sun Y, Yuan XY (2018) Magma mixing identified in the Guokeshan pluton, northern margin of the Qaidam basin: evidences from petrography, mineral chemistry, and whole-rock geochemistry. Acta Petrol Sin 34(7):1991–2016

Niu ML, Cai QR, Li XC, Yakymchuk C, Wu Q, Yuan XY, Sun Y (2021) Early paleozoic tectonic transition from oceanic to continental subduction in the North Qaidam tectonic belt: constraints from geochronology and geochemistry of syncollisional magmatic rocks. Gondwana Res 91:58–80. https://doi.org/10.1016/j.gr.2020.10.018

Parman SW, Grove TL (2004) Harzburgite melting with and without H_2O: experimental data and predictive modeling. J Geophys Res 109(B2):2003JB002566. https://doi.org/10.1029/2003jb002566

Pearce JA, Harris NBW, Tindle AG (1984) Trace element discrimination diagrams for the tectonic interpretation of granitic rocks. J Petrol 25(4):956–983. https://doi.org/10.1093/petrology/25.4.956

Peng Y (2015) The late Hercynian-Indosinian structural characteristics of the Zongwulong tectonic belt in North Qaidam Basin. Chinese Academy of Geological Sciences, Beijing

Peng Y, Ma YS, Liu CL, Li ZX, Sun JP, Shao PC (2016) Geological characteristics and tectonic significance of the Indosinian granodiorites from the Zongwulong tectonic belt in North Qaidam. Earth Sci Front 23(2):206–221. https://doi.org/10.13745/j.esf.2016.02.020

Peng YB, Yu SY, Li SZ, Zhang JX, Liu YJ, Li YS, Santosh M (2019) Early neoproterozoic magmatic imprints in the Altun-Qilian-Kunlun region of the Qinghai-Tibet Plateau: response to the assembly and breakup of Rodinia supercontinent. Earth Sci Rev 199:102954. https://doi.org/10.1016/j.earscirev.2019.102954

Petford N, Atherton M (1996) Na-rich partial melts from newly underplated basaltic crust: the cordillera Blanca batholith. Peru J Petrol 37(6):1491–1521

Polat A, Hofmann AW (2003) Alteration and geochemical patterns in the 3.7–3.8 Ga Isua greenstone belt, West Greenland. Precambrian Res 126(3–4):197–218. https://doi.org/10.1016/S0301-9268(03)00095-0

Qian B, Zhang ZW, Li WY, Jing ZC, Shao J (2018) Magma evolution and Ni–Cu sulfide mineralization potentiality of the Yanchangbeishan mafic-ultramafic intrusion in the western North Qaidam orogenic belt. Acta Petrol Sin 34(8):2275–2294

Qiu SD, Dong ZC, Gu PY (2015) The discovery of adakitic granite in the west segment of the north margin of Qaidam and its geological significance. Acta Geol Sin 89(7):1231–1243

Rapp RP, Watson EB (1995) Dehydration melting of metabasalt at 8–32 kbar: implications for continental growth and crust-mantle recycling. J Petrol 36(4):891–931. https://doi.org/10.1093/petrology/36.4.891

Reubi O, Blundy J (2009) A dearth of intermediate melts at subduction zone volcanoes and the petrogenesis of arc andesites. Nature 461:1269–1273. https://doi.org/10.1038/nature08510

Rogers G, Hawkesworth CJ (1989) A geochemical traverse across the north Chilean Andes: evidence for crust generation from the mantle wedge. Earth Planet Sci Lett 91(3–4):271–285. https://doi.org/10.1016/0012-821X(89)90003-4

Rudnick RL, Gao S (2003) Composition of the continental crust. In: Rudnick RL (ed) Treatise on geochemistry. Elsevier, Amsterdam, pp 1–64. https://doi.org/10.1016/b0-08-043751-6/03016-4

Shervais JW (1982) Ti-V plots and the petrogenesis of modern and ophiolitic lavas. Earth Planet Sci Lett 59(1):101–118. https://doi.org/10.1016/0012-821X(82)90120-0

Shi RD, Yang JS, Wu CL, Iizuka T, Hirata T (2006) Island arc volcanic rocks in the north Qaidam UHP belt, northern Tibet plateau: evidence for ocean–continent subduction preceding continent–continent subduction. J Asian Earth Sci 28(2–3):151–159. https://doi.org/10.1016/j.jseaes.2005.09.019

Shi H, Zhong C, Ma LC, Qiao JX, Hu JJ, Wei XJ (2024) Late carboniferous-early Permian sedimentary–tectonic evolution in the eastern Qaidam Basin, Western China: insight into the zircon U–Pb geochronology of ash-fall tuffs and sandstones. Mar Petrol Geol 166:106910. https://doi.org/10.1016/j.marpetgeo.2024.106910

Song SG, Niu YL, Su L, Zhang C, Zhang LF (2014) Continental orogenesis from ocean subduction, continent collision/subduction, to orogen collapse, and orogen recycling: the example of the North Qaidam UHPM belt, NW China. Earth Sci Rev 129:59–84. https://doi.org/10.1016/j.earscirev.2013.11.010

Sun SS, McDonough WF (1989) Chemical and isotopic systematics of oceanic basalts: implications for mantle composition and processes. Geol Soc Lond Spec Publ 42(1):313–345. https://doi.org/10.1144/GSL.SP.1989.042.01.19

Sun JP, Chen SY, Hu ZY, Liu WP, Guo C, Ma S (2014) Research on the mixed model and developmental characteristic of the clastic-carbonate diamictite facies in the northern Qaidam. Nat Gas Geosci 25(10):1586–1593

Sun JP, Dong YP, Ma LC, Peng Y, Chen SY, Du JJ, Jiang W (2019) Late Paleoproterozoic tectonic evolution of the Olongbuluke Terrane, northern Qaidam, China: constraints from stratigraphy and detrital zircon geochronology. Precambrian Res 331:105349. https://doi.org/10.1016/j.precamres.2019.105349

Sun GC, Gao P, Zhao ZF, Zheng YF (2020a) Syn-exhumation melting of the subducted continental crust: geochemical evidence from early Paleozoic granitoids in North Qaidam, northern Tibet. Lithos 374:105707. https://doi.org/10.1016/j.lithos.2020.105707

Sun JP, Dong YP, Jiang W, Ma LC, Chen SY, Du JJ, Peng Y (2020b) Reconstructing the Olongbuluke Terrane (northern Tibet) in the end-Neoproterozoic to Ordovician Indian margin of Gondwana. Precambrian Res 348:105865. https://doi.org/10.1016/j.precamres.2020.105865

Sun JP, Dong YP, Ma LC, Chen SY, Jiang W (2022) Devonian to Triassic tectonic evolution and basin transition in the East Kunlun-Qaidam area, northern Tibetan Plateau: constraints from stratigraphy and detrital zircon U–Pb geochronology. GSA Bull 134(7–8):1967–1993. https://doi.org/10.1130/b36147.1

Tatsumi Y (1982) Origin of high-magnesian andesites in the Setouchi volcanic belt, southwest Japan, II. Melting phase relations at high pressures. Earth Planet Sci Lett 60(2):305–317. https://doi.org/10.1016/0012-821X(82)90009-7

Taylor SR, McLennan SM (1995) The geochemical evolution of the continental crust. Rev Geophys 33(2):241–265. https://doi.org/10.1029/95rg00262

Wang YZ, Bai YS, Lu HL (2001) Geological characteristics of Tianjunnanshan ophiolite in Qinghai and its forming environment. Qinghai Geol 21(1):29–35

Wang MJ, Song SG, Niu YL, Su L (2014) Post-collisional magmatism: consequences of UHPM terrane exhumation and Orogen collapse, N. Qaidam UHPM belt, NW China. Lithos 210:181–198. https://doi.org/10.1016/j.lithos.2014.10.006

Wang XD, Hou T, Wang M, Zhang C, Zhang ZC, Pan RH, Marxer F, Zhang HL (2021) A new clinopyroxene thermobarometer for mafic to intermediate magmatic systems. Eur J Mineral 33(5):621–637. https://doi.org/10.5194/ejm-33-621-2021

Wang RT, Yang CL, Li X, Qin XS, Yuan HC, Wu SF, Wang L (2022) Zircon U–Pb isotope chronology dating of Nanshan rock mass in the Datonggou area, northern margin of Qaidam Basin and its geological significance. Geochimica 51(6):728–739. https://doi.org/10.19700/j.0379-1726.2022.06.010

Wang PL, Li YJ, Duan FH, Zhuang YJ, Zhi Q, Gu PY, Gao JP, Yang GX (2023) Petrogenesis and geodynamic setting of the Xiaosaishiteng mountain biotite monzonitic granite and quartz diorite in the western part of the northern margin of the Qaidam basin: constraints from zircon U–Pb geochronology, geochemistry and Hf isotope. Acta Geol Sin 97(10):3292–3313. https://doi.org/10.19762/j.cnki.dizhixuebao.2023358

Wang PL, Li YJ, Zhuang YJ, Gu PY, Duan FH, Lindagato P, Li H, Zhang JY, Yang GX (2024a) Middle Permian granitoids in the western section of the northern Qaidam Block, NW China: petrogenesis and tectonic implications. J Asian Earth Sci 259:105888. https://doi.org/10.1016/j.jseaes.2023.105888

Wang ZG, Sun JP, Qi YK, He WD, Ye K, Li ZL, He L, Zhang JX, Wang T (2024b) Depicting Permian to Triassic thickness variation of the Kunlun–Qaidam continental arc: implication for tectonic evolution of the south Kunlun Ocean. Acta Geochim. https://doi.org/10.1007/s11631-024-00744-9

Wang PL, Li YJ, Zhuang YJ, Gu PY, Yang GX, Duan FH, Zhang JY, Li W, Peng NH, Wang Q, Li H (2025) Carboniferous-Permian magmatism in western section of the North Qaidam, northern Tibet Plateau: response to the spatio-temporal evolution of the Paleo-Tethys Ocean. Gondwana Res 141:265–288. https://doi.org/10.1016/j.gr.2025.02.007

Wu CL, Wooden JL, Robinson PT, Gao YH, Wu SP, Chen QL, Mazdab FK, Mattinson C (2009) Geochemistry and zircon SHRIMP U–Pb dating of granitoids from the west segment of the North Qaidam. Sci China Ser D Earth Sci 52(11):1771–1790. https://doi.org/10.1007/s11430-009-0147-3

Wu CL, Wu D, Mattinson C, Lei M, Chen HJ (2019) Petrogenesis of granitoids in the Wulan area: magmatic activity and tectonic evolution in the north Qaidam, NW China. Gondwana Res 67:147–171. https://doi.org/10.1016/j.gr.2018.09.010

Wu FY, Wan B, Zhao L, Xiao WJ, Zhu RX (2020) Tethyan geodynamics. Acta Petrol Sin 36(6):1627–1674

Wu C, Zhao YH, Li J, Liu WY, Zuza AV, Haproff PJ, Ding L (2025) Multicyclic Phanerozoic orogeny recorded in the Qaidam continent, northern Tibet: implications for the tectonic evolution of the Tethyan orogenic system. Geol Soc Am Bull 137(3–4):1553–1581. https://doi.org/10.1130/b37906.1

Xia LQ, Li XM, Yu JY, Wang GQ (2016) Mid-Late Neoproterozoic to early Paleozoic volcanism and tectonic evolution of the Qilianshan, NW China. GeoResJ 9:1–41. https://doi.org/10.1016/j.grj.2016.06.001

Xu HQ, Yan YF, Qu GJ, Yuan JP, Wang QY (2019) Material composition and evolutionary characteristics of the western section of Zongwulong tectonic belt. J Qinghai Univ 37(3):87–93. https://doi.org/10.13901/j.cnki.qhwxxbzk.2019.03.014

Yan Z, Guo XQ, Fu CL, Aitchison J, Wang ZQ, Li JL (2014) Detrital heavy mineral constraints on the triassic tectonic evolution of the west Qinling terrane, NW China: implications for understanding subduction of the paleotethyan ocean. J Geol 122(5):591–608. https://doi.org/10.1086/677264

Yu SY, Peng YB, Zhang JX, Li SZ, Santosh M, Li YS, Liu YJ, Gao XY, Ji WT, Lv P, Li CZ, Jiang XZ, Qi LL, Xie WM, Xu LJ (2021) Tectono-thermal evolution of the Qilian orogenic system: tracing the subduction, accretion and closure of the Proto-Tethys Ocean. Earth Sci Rev 215:103547. https://doi.org/10.1016/j.earscirev.2021.103547

Yue Y, Sun DY, Hou KJ, Peng YB (2021) Geochronology and geochemistry of Triassic gabbro in northern Wulan, northern margin of Qaidam basin. J Jilin Univ Earth Sci Ed 51(1):154–168. https://doi.org/10.13278/j.cnki.jjuese.20190224

Zhang YM (2017) Indosinian tectonic-magmatism and regional tectonic evolution in the Qinghainanshan tectonic belt. Changan University, Changan

Zhang JP (2022) Petrogenesis and geological significance of late Permian-Middle Triassic granites in Wulan area, eastern segment of the Northern Margin of the Qaidam Basin. Hefei University of Technology, Hefei

Zhang JX, Yu SY, Mattinson CG (2017) Early Paleozoic polyphase metamorphism in northern Tibet, China. Gondwana Res 41:267–289. https://doi.org/10.1016/j.gr.2015.11.009

Zhao GC, Wang YJ, Huang BC, Dong YP, Li SZ, Zhang GW, Yu S (2018a) Geological reconstructions of the east Asian blocks: from the breakup of Rodinia to the assembly of Pangea. Earth Sci Rev 186:262–286. https://doi.org/10.1016/j.earscirev.2018.10.003

Zhao ZX, Wei JH, Santosh M, Liang SN, Fu LB, Zhao SQ, Li H (2018b) Late Devonian postcollisional magmatism in the ultrahigh-pressure metamorphic belt, Xitieshan terrane NW China. GSA Bull 130(5–6):999–1016. https://doi.org/10.1130/b31772.1

Zhao WT, Liu SF, Chen M (2020) Detrital zircon geochronology and its geological significance from Turgendaban formation in Shengge area of Zongwulong structural belt. China Miner Mag 29(S2):234–240

Zheng Y, Han J, Zhang XY, Gou ML, Wang M, Yuan BW (2024) Discovery of the Mesozoic volcanic rocks in Lahegen area of the eastern north Qaidam tectonic belt, and its geological implications: Evidence from geochemistry and zircon geochronology. Geoscience 38(4):1147–1161. https://doi.org/10.19657/j.geoscience.1000-8527.2023.074

Zhou CN, Song SG, Allen MB, Wang C, Su L, Wang MJ (2021) Postcollisional mafic magmatism: insights into orogenic collapse and mantle modification from north Qaidam collisional belt, NW China. Lithos 398:106311. https://doi.org/10.1016/j.lithos.2021.106311